Ore Geology Reviews 173 (2024) 106236

Contents lists available at ScienceDirect

Ore Geology Reviews

journal homepage: www.elsevier.com/locate/oregeorev

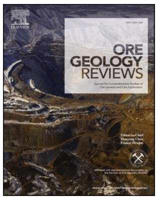

Genesis of the Rovinj-1 bauxite deposit (Istria, Croatia): Record of palaeoclimatic trends and palaeoenvironmental changes during the latest Jurassic of the Adriatic Carbonate Platform

Ivor Perković [a], Blanka Cvetko Tešović [b], Maja Martinuš [b], Igor Vlahović [a], Ivan Razum [c], Srečo D. Škapin [d], Darko Matešić [a], Milan Mihovilović [e], Tianchen He [f,g], Robert J. Newton [f], Goran Durn [a,*]

[a] University of Zagreb, Faculty of Mining, Geology and Petroleum Engineering, HR-10000 Zagreb, Croatia
[b] University of Zagreb, Faculty of Sciences, Department of Geology, HR-10000 Zagreb, Croatia
[c] Croatian Natural History Museum, HR-10000 Zagreb, Croatia
[d] Jožef Stefan Institute, Advanced Materials Department, SI-1000 Ljubljana, Slovenia
[e] GEO-5 d.o.o., HR-52210 Rovinj, Croatia
[f] University of Leeds, School of Earth and Environment, LS2 9JT Leeds, UK
[g] Hohai University, College of Oceanography, 210024 Nanjing, China

ARTICLE INFO

Keywords:
Karst bauxites
behaviour of REE and trace elements during bauxitisation
Regional unconformities
Climate aridification during the late Tithonian in the Tethyan realm
Palaeoenvironmental and redox changes during the transgression of karst terrains

ABSTRACT

Bauxites are an excellent indicator of tropical palaeoclimate and subaerial exposure in the geologic record, where the study of their structures, textures, mineralogy, geochemistry, and cover deposits can provide invaluable insight into the palaeoclimatic and palaeoenvironmental conditions during their formation. The present study focuses on these aspects of the bauxite and its cover from the Rovinj-1 deposit with the aim of reconstructing the evolution of the palaeoclimate and palaeoenvironments during its formation.

The Rovinj-1 deposit formed during the early Kimmeridgian to late Tithonian subaerial exposure phase on the Istrian part of the Adriatic Carbonate Platform (AdCP). The bauxite formation can be divided into two phases: (1) the formation of pelitomorphic bauxite under humid tropical climate, and (2) the erosion and redeposition of bauxite at the end of its formation due to climatic aridification. The climate aridification also led to increased iron oxide formation, which scavenged numerous trace elements, especially light and middle rare earth elements, causing their increase in the upper part of the deposit. The upper part also exhibits negative Ce anomalies, while the lower part displays high Ce anomalies. The bauxite formation was followed by an internal transgression during which a karstic lake formed above the bauxite. At the beggining of the transgression, the deposition of the alternation of limestones and clays started under anoxic to euxinic conditions, and equivocal to oxic conditions towards the end of the transgression, indicating the shift in lake conditions from restricted to open which is also supported by the presence of glauconite as this reflects the increasing marine influence. This sequence was interpreted as a blue hole sequence. The clays/marls of the cover sequence also reflect climatic aridification as they show a gradual increase in mixed-layer illite–smectite and illite content and a decrease in kaolinite content. The end of this regional subaerial exposure phase and the restoration of full-marine carbonate deposition is marked by the deposition of the limestones of Kirmenjak unit covering the bauxite deposit. Overall, this study enabled a detailed palaeoclimatic and palaeoenvironmental reconstruction of the Istrian part of the AdCP, expanding the current knowledge of the conditions at the AdCP during the Late Jurassic.

1. Introduction

Bauxites are divided into two types according to their respective bedrock: lateritic bauxites, which form on aluminosilicate-bearing rock through its weathering, and karst bauxites, which form on carbonate bedrock from the weathering and accumulation of aluminosilicate

---

* Corresponding author.
E-mail address: goran.durn@rgn.unizg.hr (G. Durn).

https://doi.org/10.1016/j.oregeorev.2024.106236
Received 1 March 2024; Received in revised form 25 July 2024; Accepted 8 September 2024

materials (Bardossy, 1982; Combes and Bardossy, 1995). The process of bauxitisation is a result of chemical weathering in a humid tropical to subtropical climate (Bardossy, 1982; Combes and Bardossy, 1995; D'Argenio and Mindszenty, 1992, 1995; Mindszenty et al., 1995) for extensive periods of time, usually longer than 100 Ka (Bardossy, 1982; Birkeland, 1984). Since their formation requires prolonged periods of subaerial exposure, their formation has also been largely linked to periods of tectonic instability (D'Argenio and Mindszenty, 1995; Mindszenty et al., 1995). The periods of widespread bauxite formation are linked to the global periods of elevated humidity, temperature and volcanism (D'Argenio and Mindszenty, 1992; Mindszenty, 2016). As such bauxites have been extensively used in palaeoclimatic and geotectonic reconstructions in numerous studies (Brlek et al., 2021; Chanvry et al., 2020; Ellahi et al., 2017; Mongelli, 1997; Mongelli et al., 2015; Yang et al., 2022; Zhou et al., 2023). Transgression usually follows the formation and deposition of bauxites (Bardossy, 1982; Šinkovec et al., 1994; Chanvry et al., 2020; Trabelsi et al., 2021), during which a transgressive cover-sequence is deposited over the bauxite. The bauxite cover may also contain useful information about the climatic and environmental changes that followed the formation of bauxite, and therefore several studies have focused on examining the bauxite cover to gain additional insight into the changes that followed the formation of bauxite deposits (Chanvry et al., 2020; Trabelsi et al., 2021), but most studies focus mainly or exclusively on the bauxite. Bauxites represent an end-product of chemical weathering, and as such they are composed of Al, Fe and Ti oxides, which are generally immobile and concentrated during bauxitisation. During this process, other immobile elements are also concentrated, many of which are considered as critical raw materials (Mongelli et al., 2014, 2017, 2021; Radusinović et al., 2017; Yang et al., 2019; Abedini et al., 2020a,b; Radusinović and Papadopoulos, 2021). Rare earth elements (REEs) are one such group of elements whose geochemistry and mineralogy in bauxites have been extensively studied to better understand their behaviour and enrichment in bauxites, but also to better understand the evolution of bauxites as they respond to physicochemical changes, intensity of chemical weathering, acidity and redox condition (Maksimović et al., 1991; Maksimović and Pantó, 1991; Mongelli, 1997; Mameli et al., 2007; Zarasvandi et al., 2012; Abedini and Calagari, 2014; Mongelli et al., 2014, 2017; Ellahi et al., 2017; Yuste et al., 2017; Chen et al., 2018; Abedini et al., 2018, 2019; Reinhardt et al., 2018; Yang et al., 2019; Tomašić et al., 2021; Khosravi et al., 2021; Villanova-de-Benavent et al., 2023).

Rovinj-1 karst bauxite deposit is one of the few deposits with ongoing bauxite exploitation which is not used in aluminium production, but as an additive in cement industry and a secondary ore in mineral wool production due to its high silica content. The deposit formed between the early Kimmeridgian and late Tithonian, and it is the largest bauxite deposit among the Upper Jurassic bauxite deposits formed in the northern part of the Adriatic Carbonate Platform (Trojanović, 1973; Šinkovec, 1974; Velić and Tišljar, 1988). Transgression followed the late Tithonian subaerial exposure phase (Velić and Tišljar, 1988; Vlahović et al., 2005), which is recorded through the deposition of the immediate bauxite cover and through epigenetic changes of the bauxite in aqueous environment (Šinkovec, 1974; Velić and Tišljar, 1988; Durn et al., 2003, 2006, 2023). This deposit is also a part of a widespread Upper Jurassic bauxite belt within the Tethyan realm, which extends from Spain (Molina et al., 1991), Austria (Steiner et al., 2021) and Slovenia (Dozet et al., 1993) all the way to Montenegro (Radusinović et al., 2017; Radusinović and Papadopoulos, 2021) and Greece (Laskou and Economou-Eliopoulos, 2007; Gamaletsos et al., 2017). The timing of this regional bauxitisation event coincides with the higher temperatures recorded in the Late Jurassic (Frakes et al., 1992; Haq, 2018), as most of the Jurassic was characterised by coldhouse conditions (Frakes et al., 1992) and the rise in global eustatic sea level (Haq and Al-Qahtani, 2005; Haq, 2018). The Rovinj-1 deposit was first studied by Šinkovec (1974), who focused on the genesis of the deposit, and a few decades later by Durn et al. (2003, 2006, 2023), who also studied the evolution of its cover sequence.

New petrological, mineralogical, and geochemical data of the bauxite and its cover from the Rovinj-1 deposit are presented here to provide a more detailed genetic model of the deposit and the transgression that followed its formation. The clay mineralogy of both the bauxite and its immediate cover will be studied in detail to better assess the palaeoenvironments and palaeoclimate in which the bauxite and its cover formed, as clay minerals are excellent at recording palaeoenvironmental and palaeoclimatic changes (Wignall and Ruffell, 1990; Ruffell et al., 2002; Hesselbo et al., 2009; Kovács et al., 2013; Błażėjowski et al., 2023). Particular attention will be paid to the evaluation of REE behaviour during bauxite formation and to the changes in their behaviour during the flooding of the bauxite and the formation of the immediate bauxite cover, which should lead to a better understanding of the processes that influenced the genesis of the Rovinj-1 deposit. Overall, this study will contribute to the current knowledge of the behaviour of rare earth elements during the formation of karst bauxites and their subsequent flooding. It will also improve the current understanding of the palaeoenvironments and palaeoclimatic changes that characterised the Late Jurassic subaerial exposure phase in the northwestern part of the Adriatic Carbonate Platform (AdCP) and its end, which should overall improve the current picture of the geological framework and palaeoclimate that led to the widespread Late Jurassic bauxitisation in the Tethyan realm.

2. Geological setting and the description of the Rovinj-1 deposit

Istria is the largest Croatian peninsula, predominantly built of carbonate and clastic deposits, ranging in age from Middle Jurassic to Eocene and Quaternary (Fig. 1A). Only a small portion of Istria (Fig. 1B) in the NE (Ćićarija Mt. and the topmost part of the Učka Mt.) experienced substantial tectonic deformation as a part of the Dinaridic mountain belt, while the western, central, and southern Istria experienced very little tectonic disturbance, and are regarded as a relatively undeformed part of the Adria Microplate (Schmid et al., 2008, 2020; van Hinsbergen et al., 2020). Several large-scale structures are found in this generally undisturbed part of Istria – the Western Istrian Anticline which is composed of lower Bathonian to lower Eocene carbonates, the Savudrija–Buzet anticline composed mostly of Upper Cretaceous carbonates, and the Pazin Flysch Basin filled with middle to upper Eocene turbidite deposits (Vlahović et al., 2023; Velić et al., 1995 and references therein). The entire succession of Istrian deposits is divided into four depositional megasequences, with the long-lasting regional unconformities separating them (Fig. 1; Vlahović et al., 2023; Velić et al., 1995).

The evolution of the studied Upper Jurassic Rovinj-1 bauxite deposit must be discussed within the geological framework during the late Oxfordian/Kimmeridgian to late Tithonian evolution of the Adria Microplate. During this time, first compressional event was recorded in the Adria Microplate after a very long period of extensional tectonics which ended in the late Early Jurassic (Vlahović et al., 2005 and references therein). Extensive gentle folding characterised this event, which formed as the far-field expression caused by the transition from intraoceanic supra-subduction to continental obduction of ophiolites, which occurred along the NE Adria Microplate active margin (Picotti and Cobianchi, 2017 and references therein). Consequently, very different environments were established on the previously more or less uniform shallow-marine area of the AdCP (Vlahović et al., 2001). Some areas were unaffected and remained shallow-marine, while some other areas were either temporarily drowned in the form of elongated troughs which were influenced by the open sea (Vitzthum et al., 2022, and references therein) or were temporarily subaerially exposed (Vlahović et al., 2003, 2005).

One of the best examples of subaerial exposure during this time is exposed at the Rovinj-1 bauxite deposit (Figs. 2 and 3), located north of Rovinj (Fig. 1A and C). The Rovinj-1 deposit was formed during the late Oxfordian/early Kimmeridgian to late Tithonian terrestrial phase,

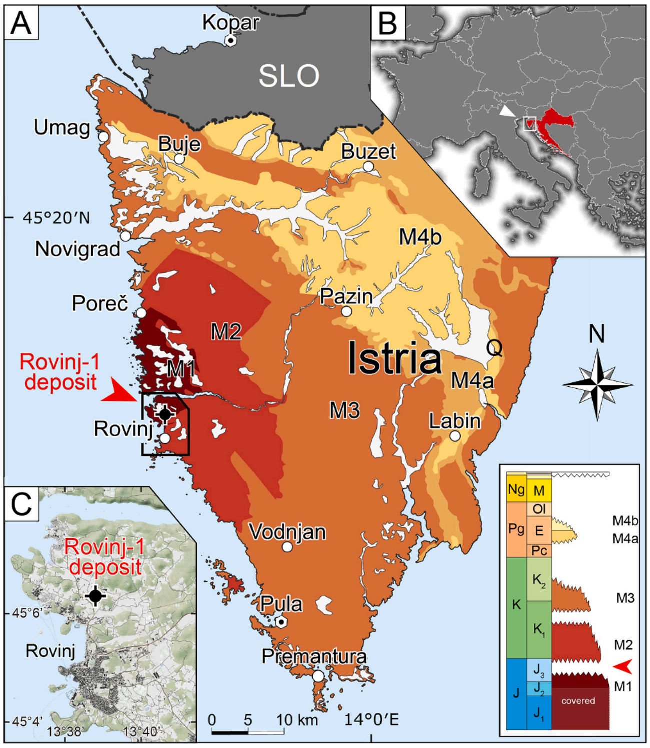

Fig. 1. Geological map of Istrian peninsula and its position in Europe. (A) Geological map of Istria, modified after Velić et al. (1995) with the schematic geological column. Legend: M1 – 1st Megasequence (lower Bathonian–lower Kimmeridgian); M2 – 2nd Megasequence (upper Tithonian–lower/upper Aptian); M3 – 3rd Megasequence (lower/upper Albian–Upper Santonian); M4a – Carbonate deposits of the 4th Megasequence (lower–middle Eocene); M4b – Clastic deposits of the 4th Megasequence (middle– upper Eocene); Q – Quaternary deposits. Position of the studied section on the chematic geological column is indicated by an arrow. (B) Map of central, western and southern Europe with the indicated location of Istrian peninsula. (C) Map of Rovinj area and geographic position of the Rovinj-1 bauxite deposit.

separating the first, lower Bathonian to lower Kimmeridgian M1 Megasequence and the second, upper Tithonian to lower/upper Aptian M2 Megasequence (Fig. 1A). The footwall of the deposit is comprised of karstified Oxfordian to lower Kimmeridgian Muča unit of the M1 Megasequence (Fig. 3), while its cover is composed of a cyclical alternation of clays/marls, black-pebble breccias and limestones, which is followed by the deposition of the upper Tithonian Kirmenjak unit of the M2 Megasequence (Fig. 3). The Muča unit comprises three lithofacies types, all indicative of the formation in high energy environment (Velić and Tišljar, 1988, and references therein): peloidal and skeletal wackestones, ooidal grainstones and ooidal and bioclastic grainstones to rudstones. The Muča unit appears as lenses within the Lim unit, which is composed of peloidal packstones deposited in a lagoonal environment (Velić and Tišljar, 1988, and references therein). Regression followed the deposition of these two units, during which the Rovinj breccias were formed locally, composed of the remnants of Lim and Muča limestones (Velić and Tišljar, 1988). Their formation was followed by the emergence, which is recorded through the formation of bauxites (Šinkovec, 1974; Velić and Tišljar, 1988), palaeosols (Velić and Tišljar, 1988; Vlahović et al., 2003; Perković et al., 2024) and on some localities as simple disconformities between the M1 and M2 Megasequences (Vlahović et al., 2003). The oscillating transgression marks the end of the subaerial exposure phase, which is best recorded in the cover succession of the Rovinj bauxite (Šinkovec, 1974; Velić and Tišljar, 1988), after which the deposition of the Kirmenjak unit started. This unit comprises a cyclical alternation of mudstones, ephemerally exposed limestones and intercalations of black pebble breccias (Tišljar, 1986; Velić and Tišljar, 1988).

The Rovinj-1 deposit contains over 15 million tonnes of bauxite on an area of approximately 40 ha (pers. comm. Milan Mihovilović), the thickness of which reaches more than 20 m and tapers outwards (Fig. 3). These features are typical of the lenticular bauxite deposits as outlined by Bardossy (1982). The deposit can be divided into two zones: (1) the sinkhole zone, where the bauxite occurs in a large sinkhole that tapers outward before being cut by normal faults (Fig. 3), and (2) the planar zone, where the main volume of bauxite occurs in a broad, strip-like bauxite body that gradually thickens toward the SE, and tapers laterally before being cut by normal faults (Fig. 3). Mining activity only takes place in the sinkhole zone, although most of the bauxite occurs in the planar zone, as the bauxite grade is much higher in the sinkhole zone. This study will only focus on the sinkhole zone as this is the only section of the deposit that was accessible for sampling. The bauxite in this zone reaches a thickness of more than 20 m in its central section, which gradually tapers to the southwest and is abruptly cut by a normal fault in the northeast (Fig. 3).

3. Materials and methods

Two profiles from the sinkhole zone were sampled for this study (Figs. 2 and 4): the main profile, which includes the thickest part of the deposit and the overlying cover, and the second, smaller profile, which includes only the contact between the uppermost bauxite and its cover. The largest dataset was collected from the main profile, which comprises

Fig. 2. Photograph of the Rovinj-1 deposit with indicated positions of the main and second profile, together with the extent of bauxite, bauxite cover and Kirmenjak unit. The direction of the photograph faces SE, while the height of the outcrop is 20 m.

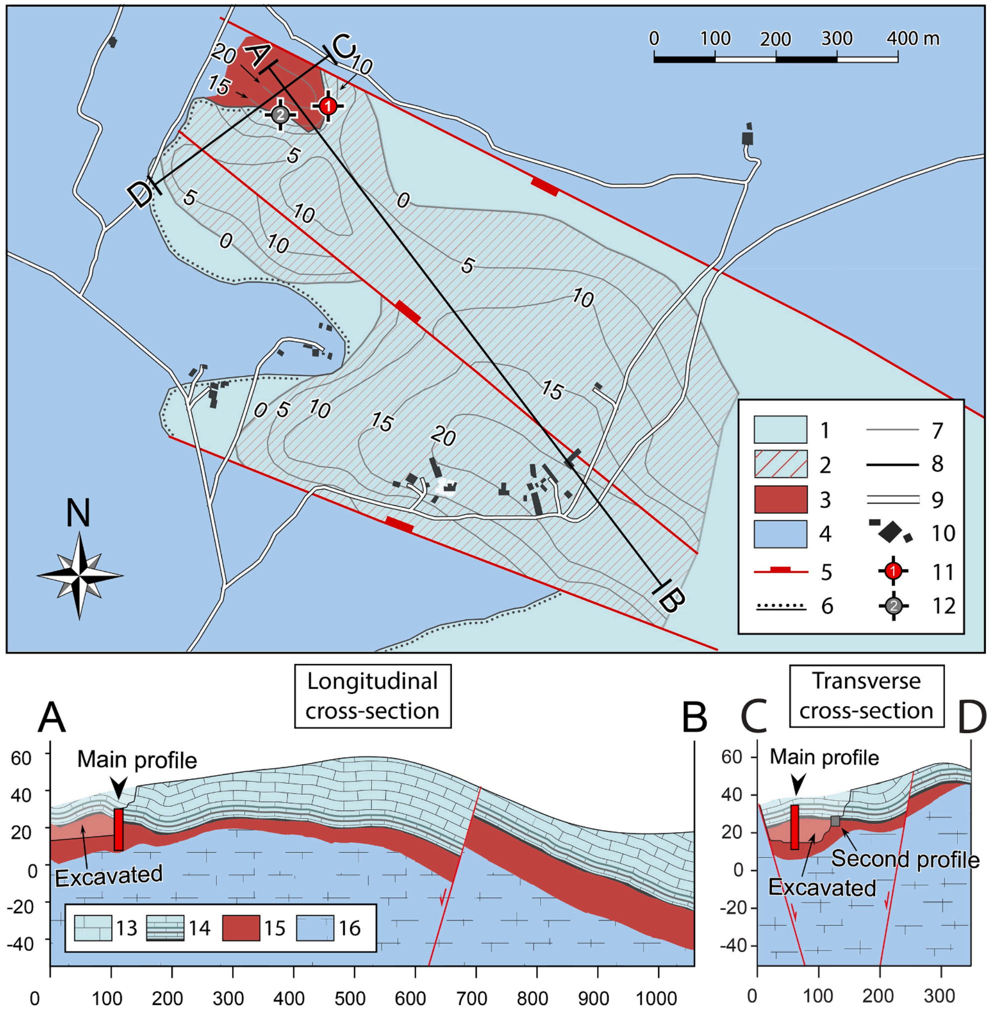

Fig. 3. Geological map of the Rovinj-1 deposit and longitudinal and transverse cross-sections (vertical scale exaggerated 3x). Legend: 1 and 14 – upper Tithonian Kirmenjak unit; 2 – bauxite covered with the Kirmenjak unit; 3 – excavated section of the Rovinj-1 deposit; 4 and 11 – Oxfordian to lower Kimmeridgian Muča unit; 5 – faults; 6 – transgressive boundary; 7 – contour lines; 8 – positions of longitudinal and transverse cross-sections; 9 – main profile; 10 – second profile; 12 – bauxite; 13 – bauxite cover.

red (R1-1 to R1-10), grey (R1-11) and white bauxite (R1-WB) samples as well as clays/marls (R1-12 to R1-19) and limestones from the cover sequence. On the main profile, the contact of the bauxite with carbonate bedrock was not sampled, due to the fact that the lower section of the bauxite was not uncovered by mining activity and was inaccessible (Fig. 2). On the second profile only the top metre of the bauxite was sampled, from which samples of grey bauxite (R2-1), clay (R2-2), clayey limestone (R2-4) and iron sulphide crusts (R2-3) were collected. This profile was sampled because it is the only accessible section of the deposit in which the uppermost part of the bauxite is not weathered and is completely preserved. From all limestone samples and bauxite samples thin sections were studied using the OPTIKA B-1000 series polarizing microscope equipped with the OPTIKA C-P6 FL camera and OPTIKA PROVIEW software. Thin sections were also prepared from separated heavy and light mineral fractions, which were separated using sodium polytungstate (SPT) solution (3.0 g/cm^3) from 250 to 63 μm granulometric fractions of seven clay/marl samples and six bauxite samples, all from the main profile. Prior to sieving, carbonates were dissolved from clay/marl samples using a 1 M NaOAc solution buffered at pH 5 with HOAc (Jackson, 1979), while iron oxides were dissolved using the Dithionite–Citrate–Bicarbonate method (Mehra and Jackson, 1960) from bauxite samples in order to liberate individual mineral grains. Micromorphological and petrographic analyses on bauxites were conducted following the guidelines outlined in Stoops (2021), while the sedimentological and micropalaeontological analyses on thick sections of limestones are based on methods by Flügel (2004).

X-ray powder diffraction (XRPD) analysis was performed on all samples, excluding the limestone samples. From each sample a smaller portion was separated, gently crushed, and passed through a 0.5 mm sieve. The following step included the milling of the sample in the McCrone micronizing mill for 15 min, for which 2 mL of the sieved material had to be mixed with 7 mL of isopropyl alcohol. The slurry that was obtained after milling was subsequently air-dried and disaggregated in an agate pestle and mortar. The dried samples were then side-loaded to produce a randomly oriented sample with uniform grain size, essential for good-quality Rietveld refinement. The Rietveld refinement was carried out using Profex version 5.2.4 software (Doebelin and Kleeberg, 2015), with the used structural data from the built-in files and crystallography open database (Graulis et al., 2009). This was used in order to obtain good-quality XRD data and semi-quantitative mineral compositions. From a portion of red bauxite and clay/marl samples the < 2 μm fraction was extracted and analysed using X-ray powder diffraction (XRPD). The <2 μm fraction from clays/marls were obtained after the dissolution of carbonate minerals, and from bauxite samples after the dissolution of iron oxides. Out of the extracted <2 μm fractions, oriented samples were prepared via dripping onto glass slides, from which diffractograms were recorded after the following treatments: (a) air-drying after Mg-solvation, (b) air-drying after K-solvation, (c) ethylene–glycol

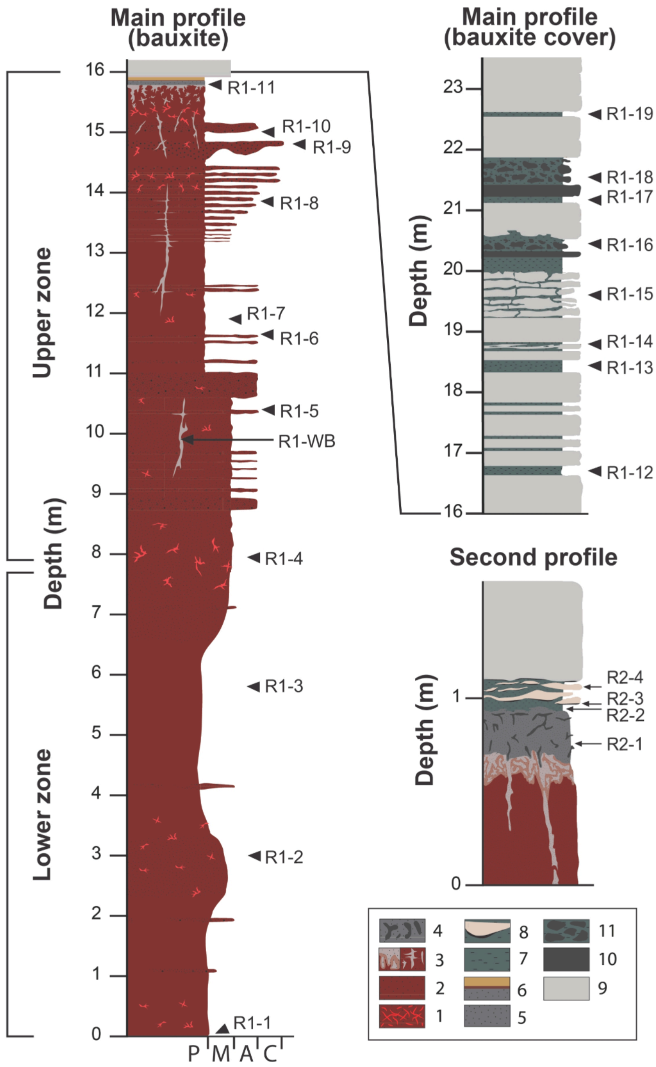

Fig. 4. Geological columns of the sampled main and second profiles together with indicated sample names and positions. 1 – clay illuviation; 2 – red bauxite; 3 – white bauxite; 4 – pyritised roots; 5 – grey bauxite; 6 – weathered clay and grey bauxite; 7 – clays/marls; 8 – clayey limestone and iron sulphide crusts; 9 – limestone; 10 – grey limestone; 11 – black-pebble breccias. Labels on the main profile (Bauxite): P – pelitomorphic bauxite; M – microclastic bauxite; A – arenitic bauxite; C – conglomeratic bauxite.

solvation after K-saturation, (d) ethylene glycol solvation after Mg-saturation, (e) solvation of K and DMSO, (f) heating for two hours at 350 °C, and (g) heating for two hours at 600 °C. The clay mineral identification was performed after Moore and Reynolds (1997) and Środoń (2006), while the semiquantitative composition of <2 µm fractions were obtained after modelling in the Sybilla© software (property of Chevron™).

For the additional analysis of clay minerals Fourier transform infrared spectroscopy (FTIR) analysis was performed on extracted <2 µm fractions. Additionally, two occurrences of green clay impregnations occurring within two clay/marl samples (R1-16 and R1-17) on the main profile were also recorded using FTIR, to determine the green clay mineral. The samples were recorded using a Bruker alpha II FTIR spectrometer and analysed in the OPUS Version 8.7 software. The absorption bands were classified and assigned to specific mineral phases and vibrational modes, where the data from Slonimskaya et al. (1986), Andersen and Brečević (1991), Madejová and Komadel (2001), and Zviagina et al. (2020) were used for the assignment of individual spectral bands to their respective vibrational modes and phases.

Additional micromorphological and geochemical data were collected using scanning electron microscopy with energy dispersive spectrometry (SEM-EDS) analysis, which was performed on five bauxite samples from the main profile. The samples were cut into centimetre-sized cubes, polished, and then subjected to detailed microstructural analysis using a field emission scanning electron microscope FE-SEM Ultra plus equipped with an energy dispersive spectrometer (EDS, Inca 400, Oxford Instruments).

To better understand the redox changes in the environment during the deposition of the bauxite cover sequence, speciation of iron was analysed, which is commonly used for the discrimination of different water-column redox conditions, from fully oxic, equivocal, through anoxic-ferruginous, to anoxic-euxinic states (Poulton, 2021; Poulton and Canfield, 2011). This is achieved through the acquisition of iron abundances in different phases, which can then be used to obtain the amount of highly reactive iron (Fe_{hr}), whose concentration relative to the total iron pool and iron-sulphide related pool (Fe_{py}) is used to reconstruct the redox conditions. Fe_{hr} comprises carbonate associated iron (Fe_{carb}), pyrite (Fe_{py}), ferric oxides (Fe_{ox}) and magnetite (Fe_{mag}). For this method, grey bauxite (R1-11 and R2-1) and clay/marl (R1-12 to R1-19 and R2-2) samples from the cover sequence were selected. The standard chemical protocol, described by Poulton and Canfield (2005), was followed during the sequential extraction of Fe_{hr} phases. For the extraction of Fe_{carb} about 65 mg of sample powder was first treated with a sodium acetate solution at pH 4.5 at 50 °C for 48 h, which was followed by the Fe_{ox} extraction using the sodium dithionite solution at pH 4.8 and room temperature for 2 h. Finally, Fe_{mag} was leached using an ammonium oxalate solution at room temperature for 6 h. After each extraction step, obtained solutions were analysed on the ThermoFisher iCE 3300 atomic absorption spectrometer (AAS) in the Cohen Geochemistry Laboratory, University of Leeds, to obtain the proportions of iron found in each iron pool. For the acquisition of Fe_{py}, the extraction using the chromous chloride distillation method (Canfield et al., 1986) was used. At the end of the extraction, silver sulphide precipitated, from whose weights the concentration of Fe_{py} was calculated stoichiometrically.

To obtain the concentrations of major, minor, trace and rare earth elements, twelve bauxite, five clay/marl samples and one sample each of clayey limestone and iron sulphide crusts were selected and sent for geochemical measurements to the commercial laboratory of Bureau Veritas, Canada, where the samples were analysed via inductive-coupled-plasma mass-spectrometry (ICP-MS) following the lithium metaborate/tetraborate fusion and nitric acid digestion. Total sulphur and carbon values were measured separately from the other major oxides. The values of trace elements and REE were normalised with the values of upper continental crust according to the values from Taylor and McLennan (1985). Additionally, seven clay/marl samples from the main profile were also analysed using Hitachi X-MET8000 handheld XRF, recording and averaging five consecutive measurements with the duration of 40 s. This method was used in order to obtain the amounts of total iron, which is required for the calculations involved in the iron speciation method, since three samples from the iron speciation data set were not measured using ICP-MS, which required the measurement of all seven samples in order to obtain the total iron using the same analytical method. Total organic carbon was also measured in those samples, using a LECO® carbon analyser.

Multivariate statistical analysis was also performed on geochemical data, but only on red bauxite samples. Since the data represents a compositional dataset, i.e. variables sum to a constant value, the dataset was pretreated using the central log-transformation, using the compositions package in R, to remove the constant sum constraint of the data. Two statistical techniques were used, principal component analysis (PCA) and the construction of correlation matrices. PCA was done using the stats package in R, while correlation matrices were constructed from the obtained Pearsons ρ values and were sorted using hierarchical clustering based on Ward's method, which was all performed using the corrplot package in R (Wei and Simko, 2017). The used cutoff p-value was 0.05, below which the individual elemental correlations were considered statistically insignificant.

4. Results

4.1. Outcrop and sample description

The bauxite in the Rovinj deposit is mainly red and cross-cut by veins of white bauxite (Figs. 2 and 4), which are more abundant in the topmost section of the deposit, where they represent a relic of the root-mat related to the bauxite palaeosurface (Fig. 4). The white bauxite veins represent mottling around the roots, which is also supported by the occasional presence of pyritised root remains within the white bauxite veins (Fig. 4). Based on macroscopic bauxite structure, the bauxite main profile can be divided into two zones: (1) the lower zone corresponding mostly to the lower half of the deposit, mainly composed of

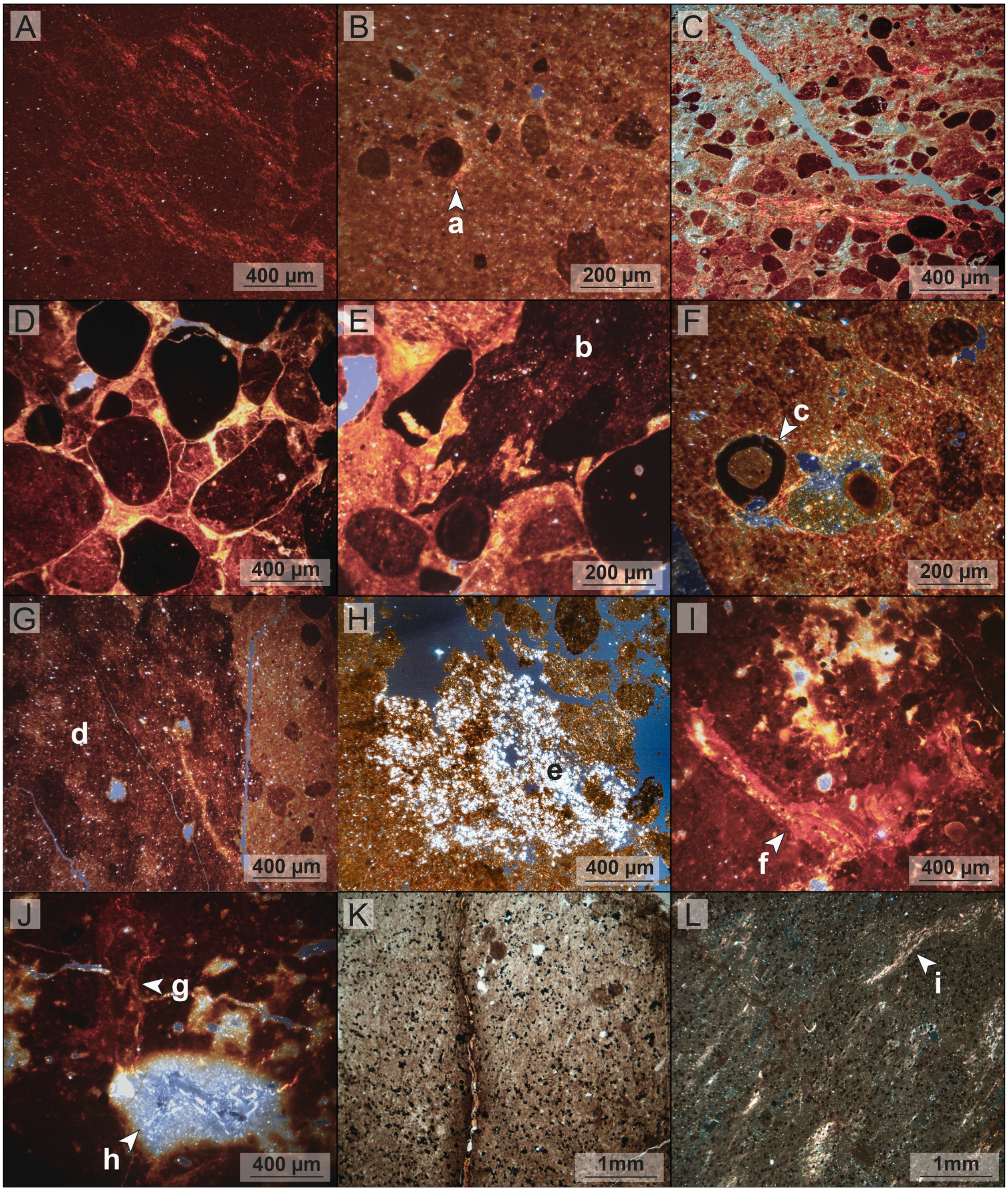

Fig. 5. Photomicrographs of the bauxite in cross- (XPL) and plane-polarised light (PPL). (A) – Pelitomorphic bauxite with clear clay coatings and parallel-striated b-fabric, sample R1-3 (XPL). (B) Iron oxide-rich bauxite grains in a pelitomorphic matrix with visible granostriation (a), sample R1-7 (PPL). (C) Arenitic to microclastic bauxite with deferrified matrix, sample R1-8 (XPL). (D) Iron oxide-rich bauxite grains in the arenitic to conglomeratic bauxite, sample R1-9 (PPL). (E) Arenitic bauxite with iron oxide impregnation (b), sample R1-10 (PPL). (F) Pseudooid with iron-oxide rich cortex (c) together with visible granostriation around bauxite grains, sample R1-7 (XPL). (G) Iron oxide impregnation (d) and its fragments in pelitomorphic bauxite, sample R1-10 (PPL). (H) Gibbsite nest (e), sample R1-4 (XPL). (I) Clear and silty clay coating (f) in pelitomorphic to microclastic bauxite with visible deferrification features, sample R1-8 (PPL). (J) Clear clay coatings (g, h) with accompanying deferrification (h), sample R1-8 (XPL). (K) Grey bauxite with dispersed pyrite grains in the matrix, sample R1-11 (PPL), (L) Grey bauxite with visible authigenic kaolinite growth (i). sample R1-11 (XPL).

pelitomorphic to microclastic bauxite with rare intercalations of arenitic bauxite (samples R1-1 to R1-3, Fig. 4) and (2) the upper zone, corresponding roughly to the upper half of the deposit, composed of the alternation of arenitic, conglomeratic and pelitomorphic to microclastic bauxite layers, with a coarsening-upward trend (samples R1-4 to R1-11, Fig. 4). In the contact of the bauxite and carbonate bedrock the bauxite is underlain with a 10-metres-thick bauxitic clay (pers. comm. Milan Mihovilović), which was unfortunately not sampled, since this section was not available during the sampling performed for this study. In the uppermost section of the bauxite, overlying the root-mat, about 0.2–0.5 m of grey bauxite is found, which contains pyritised root remains (Fig. 4). Grey bauxite gradually transitions into c. 0.2 m thick grey clay intercalated with decimetre-thick clayey limestone lenses, encrusted by centimetre-thick iron sulphide crusts. This section marks the end of the bauxite deposition and the beginning of cover sequence, and it is weathered on the main profile, so the additional second profile was sampled where the contact of the bauxite and its cover is preserved and accessible. The cover sequence comprises the 8-metres-thick alternation of few centimetre to 0.3 m thick clays/marls with limestones, brecciated regoliths and black-pebble breccias, as seen on the main profile (Fig. 4). The cover sequence of the deposit is overlain by lagoonal limestones of the Kirmenjak unit (Fig. 3).

4.2. *Petrography*

Structural bauxite types observed during profile sampling were also confirmed by petrography with the additional insight into different textures, grain types and features too small to be observed in hand specimens. Pelitomorphic to microclastic bauxite (sensu Bardossy, 1982) is composed of a cryptocrystalline matrix consisting of aluminium oxides, clay minerals and iron oxides, containing variable amounts of 10–60 μm iron-rich bauxite clasts or reworked iron oxide impregnations (Fig. 5A and B). The cryptocrystalline matrix exhibits random-striated, cross-striated, porostriated and grano-striated b-fabric (Fig. 5A and B) sensu Stoops (2021). Porostriation is observed along ped boundaries together with clear clay coatings (Fig. 5A), being a result of bauxite compaction, which also produced granostriation along different fabric elements. Arenitic to microclastic bauxite (Fig. 5C) differs from pelitomorphic to microclastic bauxite in the abundance of different grains ranging in size from 60 to 200 μm and is usually matrix-supported. Arenitic to conglomeratic bauxite is the same as arenitic bauxite, but exclusively clast supported (Fig. 5D and E), with the grains usually between 500 to 1500 μm in size, but larger grains up to 4 – 5 mm are also present. Grains in arenitic to conglomeratic bauxite are mostly represented by iron oxide-rich bauxite roundgrains, reworked iron oxide impregnations (Fig. 5D and E) and sporadically pseudooids (Fig. 5F), sensu Bardossy (1982). Pseudooids in this deposit mainly contain a bauxite roundgrain in its core (which is in places deferrified) and are always enveloped with iron oxide cortex (Fig. 5E). In situ iron oxide impregnations are mainly present in the upper section of the deposit, where they envelop grains and other fabric elements (Fig. 5E) or are present within the matrix as bands or areas rich or completely composed of iron oxides (Fig. 5G). Gibbsite crystals are in places found in association with iron impregnations, but they also occur rarely as nests within the matrix (Fig. 5H). Clay and silty clay coatings are found throughout the main profile in red bauxite (Fig. 5I and J) and are locally related to iron depletion (Fig. 5J). Grey bauxite was also subjected to the remobilisation of iron, but here iron oxides were replaced by 10–60 μm-sized iron sulphide clusters and impregnations, disseminated uniformly throughout the matrix (Fig. 5K and L). Grey bauxite also hosts undulating bands of parallel-oriented kaolinite crystals within the matrix (Fig. 5L), but these features do not exhibit a sharp contact with the matrix or grains, indicating their in situ formation. As such they are interpreted as authigenic kaolinite growth during resilification along fluid pathways. In all bauxite samples, irrespective of their colour, structure or texture, a mixture of 5–20 μm mineral grains is observed, mainly composed of mica platelets, kaolinite, quartz and sporadic occurrences of zircon and apatite. They are seen in most photomicrographs as uniformly dispersed white speckles in the bauxite matrix (Fig. 5A, B, F and G). Additional minerals were observed in the heavy mineral fraction such as clinozoisite, garnet, kyanite and hornblende, while the presence of apatite and zircon was also confirmed (Fig. 6A–E). Epidote was also found (Fig. 6F), but only in the overlying clays. Within the light mineral fraction calcite, quartz and feldspars were detected (Fig. 6G).

The carbonate samples were studied separately from the bauxite samples, with the main focus being on the analysis and description of microscopic lithological features and fossil assemblages. The lithology of the limestones is predominantly uniform, represented by peloidal to bioclastic wackestone (Fig. 7A) and bioclastic to peloidal wackestone (Fig. 7B and C) with varying amounts of allochems as well as sporadic occurrences of fenestrae (Fig. 7B). Bioclasts mainly comprise reworked ostracod shells, *Charophyta* oogoniums and rare occurrences of miliolid foraminifera (Fig. 7B and C), while some peloids represent *Favreina* coprolites (Fig. 7A). The limestones are frequently cross-cut with calcite veins, and in places with iron sulphide veins (Fig. 7D), especially abundant in the lower half of the cover sequence. Samples with pyrite veins are also accompanied by large iron sulphide clusters, mainly between 0.5 and 5 mm in diameter, the most abundant in the first few meters of the cover sequence (Fig. 7D). Laminar textures were also observed throughout the cover sequence.

4.3. *XRPD*

Determination of bulk mineralogical composition of studied samples was primarily based on XRPD, which was used for identification of present mineral phases and their variations along the studied profiles. The red bauxite is mainly composed of boehmite, kaolinite and haematite with smaller amounts of hydroxy-interlayered vermiculite (HIV) and titanium oxides (Fig. 8). Bauxite composition on the main profile is very uniform, although a slight increase in kaolinite can be observed in the topmost and lowermost sections, and a slight increase in boehmite and HIV in the middle section of the bauxite profile (Fig. 8). Grey bauxite is composed of kaolinite, boehmite, pyrite, titanium oxides, illite, HIV, and sulphate minerals (Fig. 8) on both the main and second profile, and it contains more kaolinite than the red bauxite from the main profile. The clays that overlie the bauxite are composed of kaolinite, illite, mixed-layer illite–smectite (MLIS), calcite and minor amounts of HIV, sulphate minerals, boehmite, titanium oxides, pyrite, and marcasite (Fig. 8). The clay minerals from these clays/marls exhibit a decrease in kaolinite content, coupled with an increase in illite and MLIS content. The clayey limestone is primarily composed of calcite, with minor amounts of kaolinite and traces of illite (Fig. 8), while the iron sulphide crusts are primarily composed of pyrite and marcasite, with moderate amounts of kaolinite, sulphate minerals and calcite (Fig. 8).

Study of clay minerals was based on the observations made on x-ray diffractograms of <2 μm fraction of two sample sets from the main profile: the clays/marls in the cover sequence from the main and second profile and red bauxite. Bauxite samples are composed from poorly- and well-crystallised kaolinite, hydroxy-interlayered vermiculite (HIV), illite, anatase and boehmite (Fig. 9A and B). Poorly crystalline kaolinite was determined after treatment with DMSO, where a major portion of 7 Å peak shifted towards 11.2 Å, which is indicative of well-crystalline kaolinites, while the remaining 7 Å peak was attributed mainly to poorly-crystalline kaolinite (Fig. 9A). The presence of HIV was confirmed by the collapse of 14.3 Å peak towards lower spacings after heating to 350 and 600 °C, during which it collapsed onto 13.5 Å and 12.6 Å, respectively (Fig. 9A and B), which is indicative for such clay minerals (Georgiadis et al., 2020 and references therein). The HIV does not contract after K-saturation (Fig. 9A), suggesting that it contains a high degree of hydroxy-interlayering, and does not swell after ethylene glycol saturation after Mg-saturation (Fig. 9B), which indicates that the

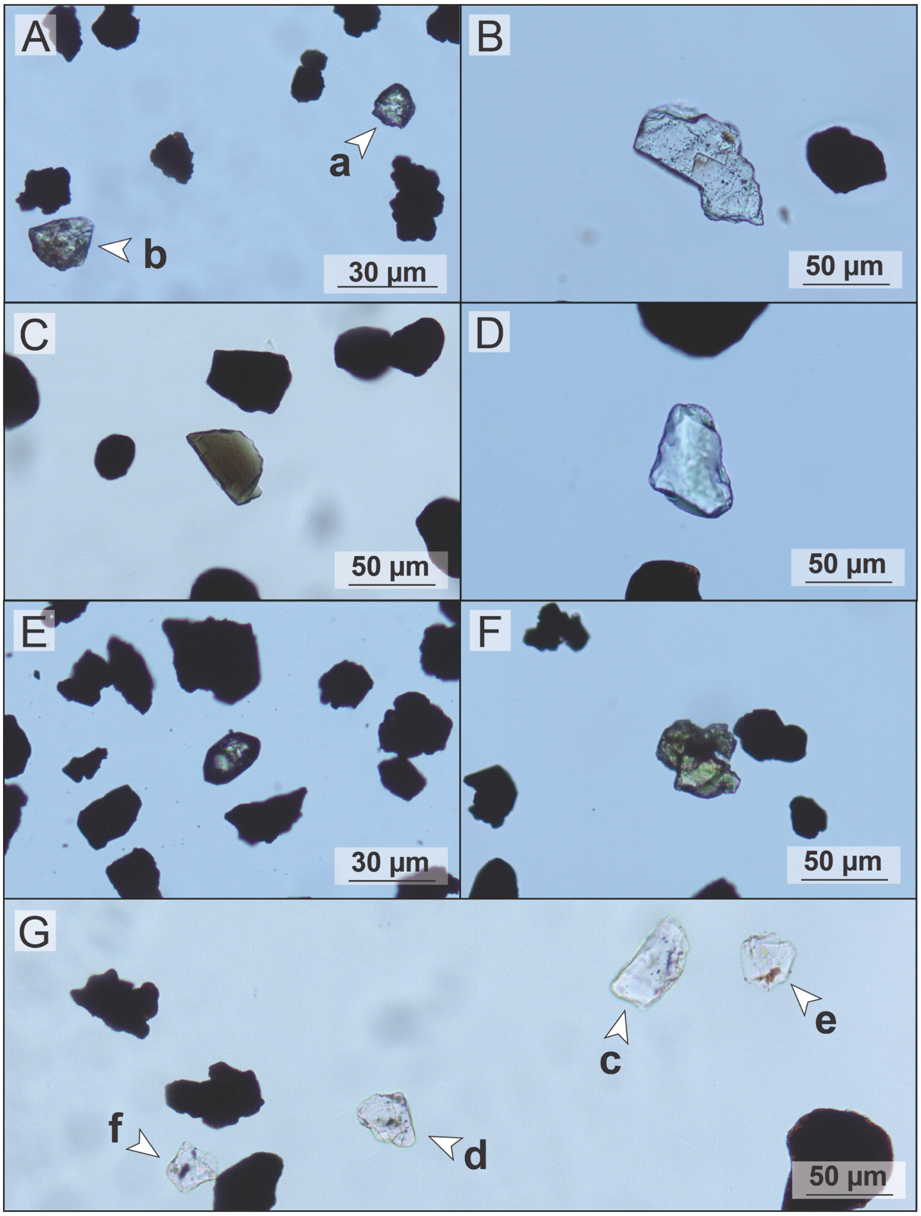

Fig. 6. Photomicrographs of transparent mineral grains from heavy and light mineral fractions in plane-polarised light. (A) Clinozoisite (a) and garnet (b). (B) Kyanite. (C) Amphibole. (D) Apatite. (E) Zircon. (F) Epidote. (G) Quartz (c, d) and feldspars (f, e).

observed phase is a hydroxy-interlayered vermiculite and not a hydroxyl-interlayered smectite minerals (Georgiadis et al., 2020 and references therein). During modelling in Sybilla, diffraction maxima of boehmite and anatase were excluded from the calculation since structures other than clay minerals cannot be modelled in Sybilla, and the focus of the modelling was the acquisition of relative proportions of different clay minerals along the bauxite profile. The HIV model was approximated using the chlorite structure with low interlayer cation content. Towards the lower section of the bauxite profile, an increase in HIV and illite can be observed, accompanied with the slight decrease in kaolinite content (Fig. 10).

The <2-µm fractions from cover clays/marls contain similar clay minerals as in the bauxite samples, with the addition of MLIS (Figs. 9C, D and 10). HIV displays the same characteristics as in the bauxite (Fig. 9C and D), but in one sample it shifts towards 13.6 Å after heating to 600 °C, indicating that it contains a higher degree of hydroxy interlayering compared to the other samples. The MLIS is characterised by a broad illite(001)/smectite(001) peak located at approximately 11.5 Å in air-dried Mg-saturated state (Fig. 9D), which contracts towards 10.3 Å upon K-saturation (Fig. 9C), which is characteristic for vermiculite as it transforms into illite-like structure after K-solvation (Moore and Reynolds, 1997; Środoń, 2006), which is also supported by no change after ethylene glycol solvation and K-saturation (Fig. 9C). Upon ethylene glycol solvation and Mg saturation, this peak shifts to approximately 15 Å (Fig. 9D), which is characteristic for smectite (Moore and Reynolds, 1997; Środoń, 2006). The fact that the smectite interlayers in MLIS display behaviour characteristic for both smectites and vermiculites, indicates that this phase is a high-charge smectite. In the ethylene glycolated Mg-saturated sample (Fig. 9D), the illite(001)/smectite(002) peak appears at about 9 Å, which coupled with the presence of a 15 Å illite(001)/smectite(001) peak indicates a degree of ordering in the MLIS (Środoń, 1980, 1981; Moore and Reynolds, 1997). This was also established by modelling in Sybilla, where a R2 ordered MLIS model with approximately 85 % of illite layers provided the best fit on X-ray diffractograms of ethylene glycol-solvated and air-dried samples. This phase is therefore characterised as a R2 illite/smectite with 85 % of illite

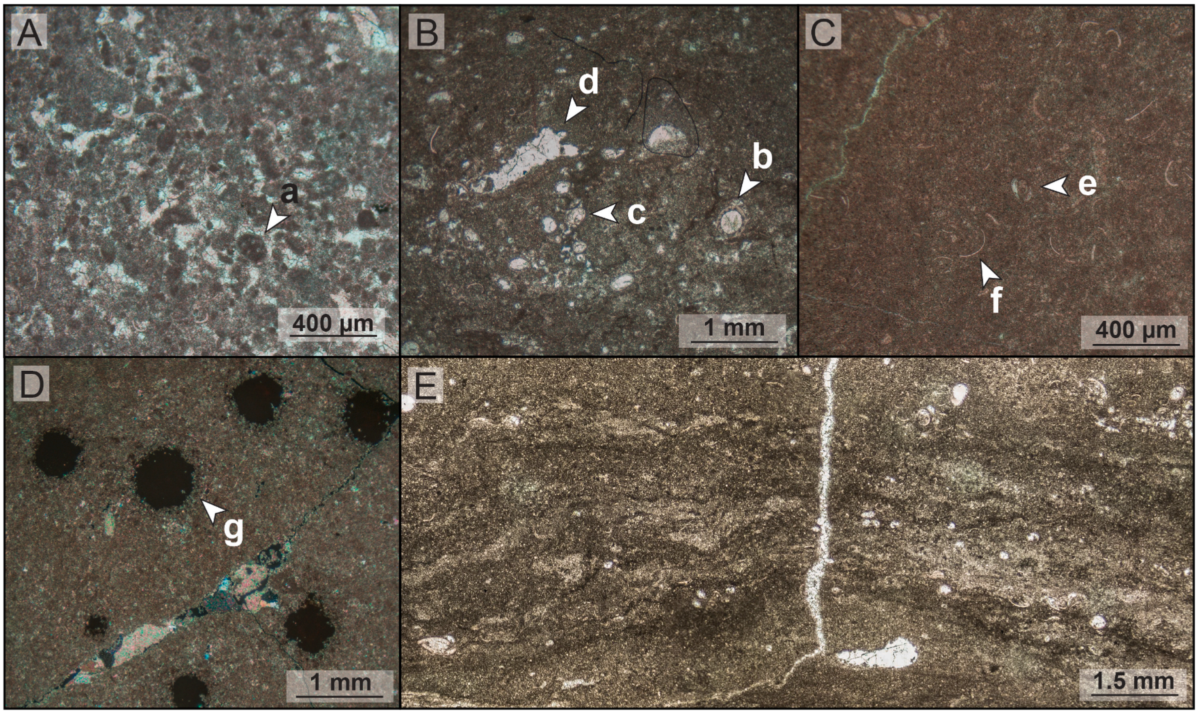

Fig. 7. Photomicrographs of limestones from the cover sequence cross- (XPL) and plane-polarised light (PPL). (A) *Favreina* peloid (a) in a peloidal wackestone, XPL. (B) Bioclastic wackestone with *Charophyta* oogoniums (b), ostracods (c) and fenestrae (d), PPL. (C) Milliolid test (e) and ostracod shells (f) in bioclastic wackestone, PPL. (D) Iron sulphide crystal clusters (g) and calcite veins in peloidal wackestone, XPL. (E) Laminar texture in bioclastic to peloidal wackestone, PPL.

layers. The acquisition of relative proportions of clay minerals through modelling in Sybilla indicated a clear trend observed in the clays/marls of the cover sequence: the kaolinite proportions decrease towards the upper part of the cover sequence, which is coupled by the increase in MLIS and illite, while the proportions of HIV do not display a significant trend (Fig. 10).

4.4. FTIR

The clay mineralogical data obtained from XRPD were coupled with FTIR measurements in order to gain additional information about the structural and chemical properties of clay minerals found in bauxite and clay/marl samples. Presence of illite was indicated by the presence of 3620, 1088, 835, 697, and 523–533 cm^{-1} bands in the absorption spectra (Table 1; cf. Slonimskaya et al., 1986; Zviagina et al., 2020). Illite is dioctahedral, as most of the bands are aluminium-related, but the presence of magnesium in its structure was also confirmed, as indicated by the 830 cm^{-1} Al-OH-Mg stretching band (Table 1). Illites in R1-17 and R1-18 samples were found to contain some iron, as the shift of the δ_3 Si-O-Si band towards 523 cm^{-1} (Table 1) indicates the presence of iron in the structure of illites (Zviagina et al., 2020). From these samples green clay impregnations were separated and analysed and were confirmed to be composed of glauconite, as indicated by the presence of 3570, 3531, 3506, 1020, 824, 668 and 517 cm^{-1} bands (Table 1). The mineral was identified as glauconite based on its very broad band character (Slonimskaya et al., 1986) and presence of both ferric and ferrous iron indicated by 3568, 3527, 3507 and 827 cm^{-1} bands (Table 1; cf. Zviagina et al., 2020). Glauconite was only studied using FTIR, since very small amounts were possible to collect. Kaolinite was detected by the presence of 3697, 3653, 3623, 1009, 939 and 539 cm^{-1} bands (Table 1; cf. Madejová and Komadel, 2001), and was determined to be primarily represented by disordered kaolinite, since the 3669 and 3652 cm^{-1} bands detected in well crystallised kaolinite are replaced with a single band located at 3653 cm^{-1} in poorly-crystalline kaolinites (cf. Russell and Fraser, 1994). Calcite was detected only in clay/marl samples, by the presence of 1428, 876 and 711 cm^{-1} bands (Table 1: cf. Andersen and Brečević, 1991). Boehmite was detected by the presence of 3287, 3098, 2095, 1971, 1156 and 675 cm^{-1} bands (Table 1; cf. Kiss et al., 1980).

4.5. SEM-EDS

SEM-EDS measurements were mainly used for the micromorphological study of observed mineral phases and for the detection of minor phases which could not have been determined using XRPD and conventional petrography. Mainly studied was micromorphology of kaolinite, which was rarely found to be present as few micrometre-sized vermiform-like crystals (Fig. 11A) but is mainly present as nanoparticles, in the form of platelets few hundred nanometres or less in size (Fig. 11B), indicating its pedogenic origin. Authigenic ilmenite was also detected in one sample, as clusters of few micrometre-sized crystals (Fig. 11C). The most notable finding was a REE-bearing phase (Fig. 11D), which was found only in the lowermost sample from the main profile. This phase formed in situ, since it exhibits a gradual boundary with the matrix, and is present as impregnations or veins few hundred micrometres in size. It is composed mainly of Ce, Nd, La, Y and Ca (Fig. 11E). Detected Al, Si and Fe (Fig. 11E) do not belong to this phase but were detected because of the association of this phase with the bauxitic matrix, which was also captured in the EDS spectra. This phase is likely a carbonate REE mineral, but this could not have been definitely proved, since the samples were coated with carbon. Ca-bearing REE minerals found in bauxite are usually carbonates of the bastnaesite group (Bardossy, 1982; Maksimović et al., 1991; Mongelli, 1997; Radusinović and Papadopoulos, 2021; Tomašić et al., 2021; Villanova-de-Benavent et al., 2023), where the calcium-rich members are parisite, röntgenite and synchesite (Ni et al., 1993, 2000; Kalatha et al., 2017), which best describe the detected REE phase from the Rovinj-1 deposit.

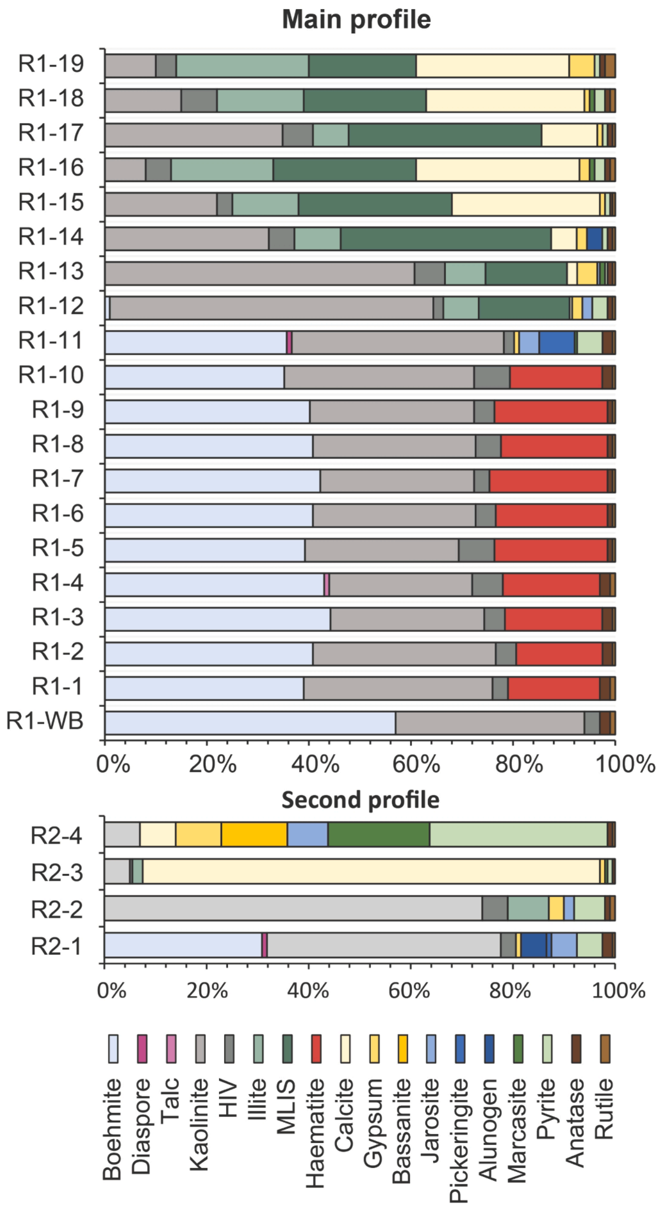

Fig. 8. Mineralogical composition of bulk samples from main and second profile.

4.6. Geochemistry

4.6.1. Major elements

The Rovinj-1 bauxite has a very uniform chemical composition, with few lesser variations. The uppermost part of the section displays a slight decrease in Al_2O_3, coupled with an increase in SiO_2 (Fig. 12). The highest Al_2O_3 values are found in the middle of this section, while the SiO_2 content increases again towards the lower part of the section (Fig. 12). TiO_2 values are generally constant, but they display variations and a slight decrease in the upper section of the red bauxite (Fig. 12). The Fe_2O_3 and P_2O_5 values increase in the red bauxite towards the top of the main profile, coupled with the decrease in MnO_2 values together with a slight decrease in K_2O and MgO values (Fig. 12). CaO, TOT/C and TOT/S show no variations (Fig. 12). The cover succession is marked by a clear trend in major oxide values, as there is a steady increase in K_2O, MgO, SiO_2, TOT/C, TOT/S followed by the decrease in Al_2O_3, Cr_2O_3 and TiO_2 (Fig. 12). Grey bauxite has a similar composition as the red bauxite but has a lower Fe_2O_3 content and elevated TOT/S content (Fig. 12). White bauxite sample has much higher Al_2O_3 and TiO_2 values, as well as lower Fe_2O_3 and SiO_2 values than the red bauxite (Fig. 12). On the second profile, the grey bauxite has almost the same composition as the grey bauxite from the main profile, with slightly lower Al_2O_3, TiO_2, Fe_2O_3 and TOT/S values, while displaying slightly higher SiO_2 values (Fig. 12). The tables with exact values can be found in the appendix.

4.6.2. Trace elements

Three main trends can be observed in the bauxite section of the main profile: (1) Cd, Co, Cu, Ga, Hf, Mo, Nb, Ta, Th, Zn and Zr have constant values, (2) Sr, U and V show an increase towards the upper section of the bauxite, and (3) Ba, Cs and Rb display a gradual increase towards the lower section (Fig. 13). With respect to UCC values (Taylor and McLennan, 1985), red bauxites are enriched in Be, Co, Ga, Ni, Pb, Sb, Sn, U, V, W, Zn and high-field-strength elements (HFSE) such as Hf, Nb, Ta, Th and Zr, as well as depleted in Bi, Cd, Se, Mo, Tl and large-ion lithophile elements (LILE) such as Ba, Rb and Sr, with the exception of Cs which is enriched (Fig. 14A). Grey bauxite generally contains similar trace element contents as the red bauxite, but it is enriched in As, Co and Cu, and slightly enriched in Mo (Fig. 14A). White bauxite differs from red bauxite by its depletion in Mo and As, and slight enrichment in U (Fig. 14A). The clayey limestone and iron sulphide crusts show a depletion in HFSE, LILE, Ga, Sn, Th, U, V and W, with the iron sulphide crusts being enriched in As, Co, Mo, Ni, Sb, Sc, Tl and Zn while the clayey limestone being enriched in As, Co, Mo and Zn (Fig. 14B). Iron sulphide crusts display the highest Mo content compared to all other sample types, and are also enriched in Co, Pb and Zn (Fig. 14B). The clay/marl samples display a depletion in LILE, with the exception of Cs which is enriched, and an enrichment in Co, Mo, Ni, Th, U and V (Fig. 14B). Several trends can be observed in the cover sequence: (1) decrease in HFSE, Bi, Ga and Sn, (2) enrichment of As, Cd, Co, Cu, Mo, Ni, Pb, Sb and Zn at the bottom of the cover sequence, (3) enrichment of As, Cu, Mo, Tl, U and V at the top of the cover sequence, and (4) a gradual increase in Sr (Fig. 13). The first clay layer (R2-2) displays a different signature compared to the rest of the cover clays/marls due to its visibly different trace elemental composition, as it is significantly more enriched in Cd, Co, Cu, Ni, Pb and Zn, and depleted in Ba, Rb and U compared to the rest of the cover clays/marls (Figs. 13 and 14B). The tables with exact values can be found in the appendix.

4.6.3. Rare earth elements

REE elements show a progressive increase towards the upper parts of the bauxite (Fig. 15), and they are much lower in the clays/marls from the bauxite cover. Two main types of REE patterns were recognised in the Rovinj-1 deposit bauxite, when evaluating their UCC and chondrite normalized patterns (Fig. 14C and D): (1) samples with lower LREE (La, Ce, Pr and Nd) and MREE (Sm, Eu and Gd) content and (2) samples with higher LREE and MREE content compared to the first type (Fig. 14C and D). The variations in $(La/Yb)_{ch}$ and $(Gd/Yb)_{ch}$ ratios (Fig. 15), which are commonly used to evaluate REE fractionation of bauxites (Mongelli et al., 2014; Yuste et al., 2017; Abedini and Khosravi, 2024), also support the observed differences in LREE and MREE content, as they are much higher in the samples of the second type (Fig. 15). HREE (Tb, Dy, Er, Ho, Tm, Yb, Lu and Y) values are constant throughout the bauxite (Figs. 14C, D and 15). Ce anomalies display significant differences along the profile, as in the upper half of the main profile slight negative to no Ce anomaly is present ($Ce/Ce^* = 0.80–1.04$, Supplementary table), while the lowermost samples exhibit a high positive Ce anomaly (Fig). Grey bauxite also has the lowest LREE and MREE content, which is also supported by lower $(La/Yb)_{ch}$ and $(Gd/Yb)_{ch}$ ratios, and also displays a slight negative Ce anomaly ($Ce/Ce^* = 0.88$, Supplementary table) on the second profile (Figs. 14C, D and 15). The clayey limestone displays an enrichment in LREE and especially in MREE (Fig. 14E and F). Clays/marls display a depletion in LREE and MREE and an enrichment in HREE and show no sign of Ce anomaly (Fig. 14E and F). The clay from the first clay layer (R2-2) is different from the rest of clay/marl samples, as it displays higher LREE and especially MREE content when evaluating the

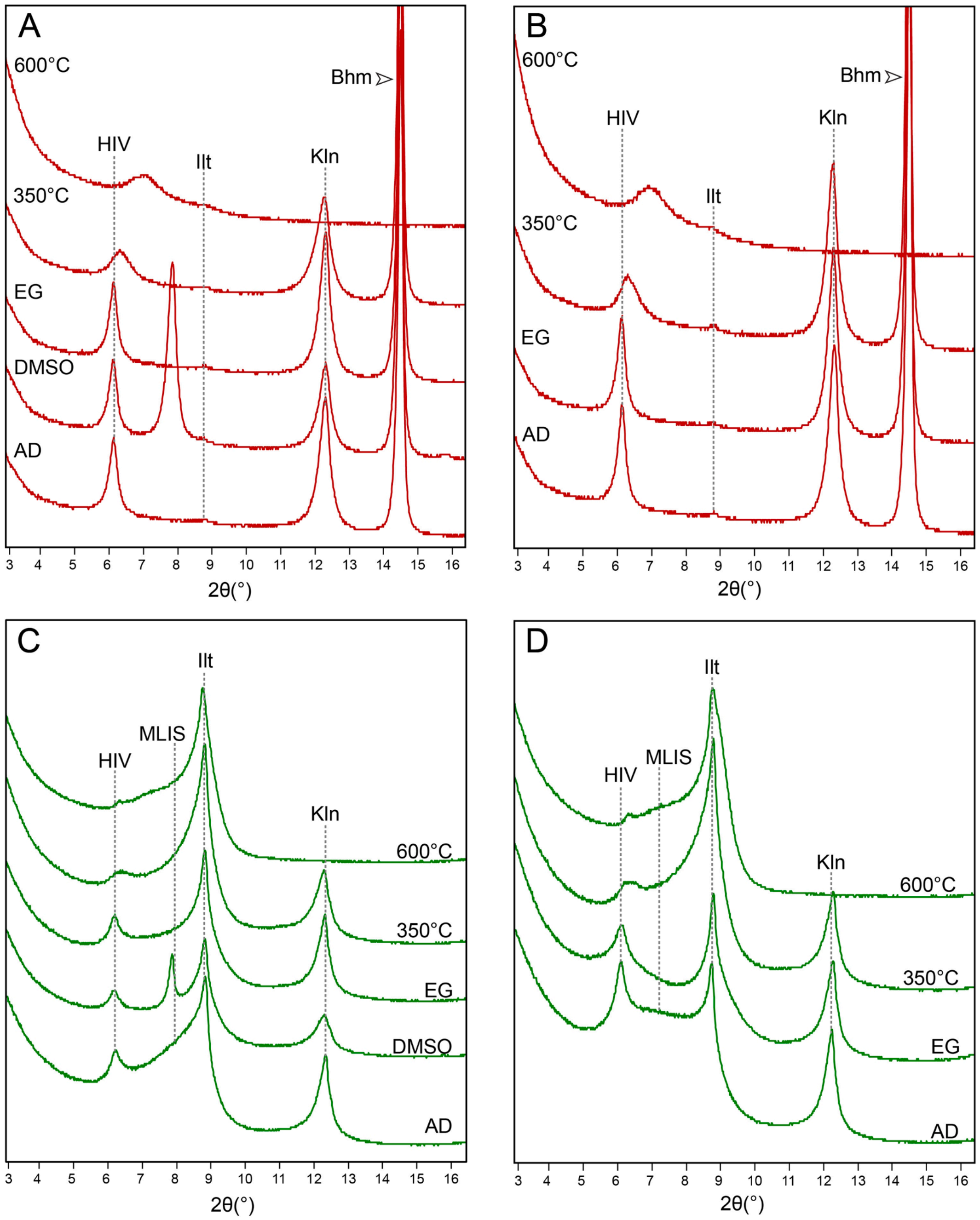

Fig. 9. X-ray diffraction patterns of <2 μm fractions recorded after diagnostic treatments. (A) X-ray diffraction patterns recorded after treatments of Mg-saturated <2 μm fraction from the R1-1 red bauxite sample, (B) X-ray diffraction patterns recorded after treatments of K-saturated <2 μm fraction from the R2-4 clay sample, (C), X-ray diffraction patterns recorded after treatments of Mg-saturated <2 μm fraction from the R2-4 clay sample, (D) X-ray diffraction patterns recorded after treatments of K-saturated <2 μm fraction from the R2-4 clay sample. Legend: AD – air dried; DMSO – dimethyl sulfoxide saturation; EG – ethylene glycol saturation; 350 °C – heating to 350 °C; 600 °C – heating to 600 °C; HIV – hydroxyl-interlayered vermiculite; MLIS – mixed-layer illite–smectite; Ill – illite; Kln – kaolinite; Bhm – boehmite (abbreviations taken from Warr (2021), except for hydroxyl-interlayered vermiculite - HIV).

UCC and chondrite normalised patterns (Figs. 14E and F) as well as higher $(La/Yb)_{ch}$ and $(Gd/Yb)_{ch}$ values (Fig. 15) compared to the other clays/marls together with a positive Ce anomaly (Figs. 14E, F and 15), although a low one ($Ce/Ce^* = 1.24$, Supplementary table). Eu anomaly exhibits a narrow range of values ($Eu/Eu^* = 0.62$–0.69, Supplementary table), and is negative throughout the bauxite profile, as well as the clays/marls (Figs. 14F and 15). There are some variations in the Eu/Eu* values, especially in the clays/marls, but they are regarded as insignificant, due to the very narrow range of Eu/Eu* values. REE elements show a progressive increase towards the upper parts of the bauxite (Fig. 15).

4.7. Multivariate statistical analysis

The behaviour of major trace and rare earth elements in bauxites from the Rovinj-1 deposit was also investigated using multivariate statistical methods. The main objective was to determine the associations of elements that behave similarly in order to evaluate their behavioural pathways and phase associations. Only red bauxite samples were selected for this step. Two principal components were used for the construction of PCA plots after the evaluation of the scree plot (Fig. 16), as PC1 and PC2 account for 79.8 % of the total variance in the dataset. Arsenic was excluded from statistical analysis due to a number of values

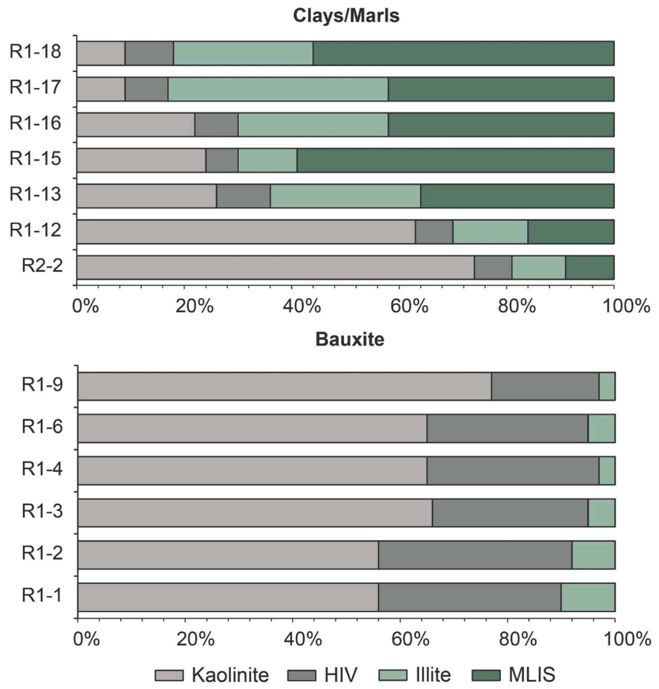

Fig. 10. Clay mineral composition of <2 μm fractions obtained from bauxite and clay/marl samples.

below the detection limit. Several clear elemental groups can be observed on the constructed PCA plot: (1) LREE, MREE; (2) HFSE, HREE, P_2O_5, Al_2O_3, Na_2O, CaO, SiO_2, Cr_2O_3, TiO_2, LOI, Bi, Cd, Ga, Pb, Se, Sn, Sr, V, and W; (3) LILE, MgO, K_2O, CaO, Na_2O and SiO_2 (Fig. 17). Ce and Cu do not show any association with these elemental groups, and do not display any correlation to other elements. The constructed correlation matrix largely supports the associations derived from the PCA, but there are some differences (Fig. 18). P_2O_5, Fe_2O_3, Sr, U, Cd and W are closely associated and show no meaningful correlation with the rest of the second group, and are also associated with S, Be, and Mo as they show a strong and meaningful mutual correlation with those elements. Zn, Ni and Tl are also grouped together and mutually correlated (Figs. 17 and 18) and they show similar variations in the bauxite (Fig. 13), likely as a consequence of their depletion in R1-6 sample, suggesting that they were influenced by similar processes and are related to the same mineral phases. Despite being associated with the second group on the PCA plot, CaO, Cr_2O, Na_2O, SiO_2, Ho, Er, Se, Bi and V do not show any mutual correlation with the rest of the elements from the second group. Y also displays some differences, as it shows a high degree of mutual correlation with LREE and some HREE, while not being strongly associated with the second group. The elements from the first group and the third group display some degree of positive correlation between them.

4.8. *Iron speciation data and TOC*

From the obtained Fe_{carb}, Fe_{py}, Fe_{ox}, Fe_{mag} and total iron (Fe_{tot}) values, Fe_{hr}/Fe_{tot} and Fe_{py}/Fe_{hr} ratios were calculated in order to evaluate the redox variations during the deposition of the bauxite cover sequence. The Fe_{hr}/Fe_{tot} ratio was used to discriminate between oxic, equivocal and anoxic depositional conditions, where the values higher than 0.38 indicated deposition under anoxic conditions, values higher between 0.22 and 0.38 indicated deposition under equivocal conditions, while the values lower than 0.22 indicated deposition under oxic conditions (Poulton and Canfield, 2011). The anoxic conditions were further evaluated using the Fe_{py}/Fe_{hr} ratio, which allows the discrimination between ferruginous and euxinic conditions, where values lower than 0.6 indicate deposition under ferruginous conditions, and those higher than 0.8 deposition under euxinic conditions (Poulton, 2021). In the bauxite cover succession, the lower part was deposited under ferruginous and euxinic conditions, and the upper part under equivocal conditions (Fig. 19). The visible trend in the Fe_{py} content displays a gradual decline from the lower part towards the upper part (Fig. 19), supporting the redox changes indicated by the Fe_{hr}/Fe_{tot} ratio. The decrease in Fe_{py} content is also coupled with the increase in Fe_{res} and Fe_{tot} content (Fig. 19), indicating that the iron was hosted primarily in other phases in the upper section of the cover sequence and not in iron sulphides. Total organic carbon is very low in both grey bauxite and the cover clays, with values below 0.2 % (Fig. 19).

5. Discussion

5.1. *Geotectonic evolution and affinity of parental material*

The formation of Rovinj-1 deposit was enabled by the emergence of the Istrian part of the AdCP in the late Oxfordian/early Kimmeridgian, when karstification of the carbonate bedrock and accumulation of parent material from which the bauxite was derived started. This uplift was tectonic in nature, and it temporally coincides with the obduction of the Vardar Ocean (Schmid et al., 2008, 2020; Picotti and Cobianchi, 2017; van Hinsbergen et al., 2020), which triggered the formation of the flexural forebulge in the foreland of the obduction zone, as this event led to the additional intraplate stress in the underlying plate which was generated by the pressure of the obducted oceanic crust of the Vardar Ocean. The formation of karst bauxites in passive plate interiors under intraplate stress was described by D'Argenio and Mindszenty (1995) and was also applied in case of the Austrian Ludberg bauxite, which was also formed during the Late Jurassic (Steiner et al., 2021).

The type and source of the parent material from which the Rovinj-1 bauxite formed is hard to pinpoint, since bauxitisation is an extremely aggressive process, leading to the loss of primary textures and original composition of the parent material. Nevertheless, the composition of its heavy and light mineral fraction, together with several petrographical observations, allowed a tentative reconstruction of the sources and types of its parent material. The occurrence of metamorphic minerals such as clinozoisite, garnet, kyanite and epidote (Fig. 6A, B, F) coupled with the presence of finely dispersed equidimensional mica, quartz and feldspar grains in the bauxite matrix (Fig. 5A, B, F, G) indicate the contribution of aeolian material during its deposition. The exact source of the aeolian material could be precisely pinpointed by the dating of detrital zircons (Kelemen et al., 2017, 2023; Brlek et al., 2021), but since this was not performed in this study, exact source of the aeolian material could not have been established. The presence of euhedral zircons likely indicates the contribution of volcanic material, which is also plausibly supported by the presence of amphiboles (Fig. 6E). There is evidence of contemporaneous volcanic activity as occurrences of several levels of bentonites/tuffs of Kimmeridgian to Tithonian age are documented in the nearby Gorski Kotar, Croatia (Šćavničar and Nikler, 1976; Velić et al., 1994, 2002) and in the Trento Plateau, NE Italy (Pellenard et al., 2013; Picotti and Cobianchi, 2017). These materials were likely derived from the volcanic centres formed during the obduction of the Vardar Ocean, as suggested by Picotti and Cobianchi (2017). The contribution of the insoluble carbonate residue cannot be overlooked, as Muča limestones, which compose the bedrock of the Rovinj-1 deposit, contain a relatively high content of insoluble residue (2.19 %; Durn et al., 1999), which was liberated and accumulated during the karstification of these limestones. Therefore, it can be concluded that the parent material from which the Rovinj-1 bauxite deposit was formed was polygenetic in origin and derived from aeolian dust, volcanic dust and insoluble carbonate residue.

The bauxite samples also display negative Eu anomalies (Fig. 15), which were likely inherited from the parent material, probably from the volcanic material or the aeolian dust, but it is hard to exactly determine and correlate them with any contemporaneous volcanic materials as

Table 1
Detected bands <2 µm fraction samples, with their respective band and mineral phase assignment. R1-16* and R1-17* are the green-clay separates from the R1-16 and R1-17 samples. Legend: Bhm – boehmite; Cal – calcite; Glc – glauconite; Ill – illite; Fe-Ill – iron-containing illite; Kln – kaolinite.

Clay/Marl <2 µm fractions									Bauxite <2 µm fractions						Assigned mineral	Assigned band
R1-19	R1-17	R1-17*	R1-16	R1-16*	R1-15	R1-13	R1-12	R2-2	R1-9	R1-6	R1-4	R1-3	R1-2	R1-1		
3699			3697	3700	3697	3697	3697	3697	3697	3697	3697	3696	3696	3696	Kln	ν AlOHAl
3650						3650	3650	3654	3653	3652	3651	3654	3654	3654	Kln	ν AlOHAl
3620	3620	3620	3621	3620	3621	3621	3621	3621	3621	3620	3621	3623	3622	3623	Ill, Kln	ν AlOHAl
	3570	3568		3568											Glc	ν AlOHFe^{2+}
3531		3528		3527											Glc	ν Fe^{2+}OHFe^{3+}
		3506		3507											Glc	ν Fe^{2+}OHFe^{2+}
3443	3454	3442	3454		3451	3449	3454	3455	3450	3450	3450					ν H_2O
3429																
3230	3248		3238		3240	3251										
									3287	3288	3288	3287	3287	3287	Bhm	ν_{as} H_2O
									3098	3099	3098	3096	3096	3096	Bhm	ν_s H_2O
									2095	2099	2095	2095	2097	2096	Bhm	
									1971	1971	1971	1970	1971	1971	Bhm	
1753		1800		1802												
1642	1639	1635	1634	4635	1635		1634	1641	1635	1633	1636	1638	1638	1638	δ H_2O	
1548																
	1462						1461	1452	1444	1456	1457					
					1440											
1428		1427		1428		1420	1420	1427							Cal	ν_3 CO_1
	1402															
1385	1384						1384	1384	1390	1385	1385					
1316										1314						
									1156	1156	1153				Bhm	δ_{as} OH
							1009	1008	1009	1110	1109	1110	1110	1110	Ill, Glc	ν SiOap
1088	1087	1084	1089	1086	1087										Glc	ν SiOap
									1080	1080	1079	1072	1072	1072	Bhm	
		1020		1020											Glc	ν SiO
1030	1032		1030		1031	1032	1032	1032	1033	1033	1033	1034	1034	1034	Kln, Ill	ν SiO
						1009	1008	1007	1008	1008	1008	1009	1009	1009	Kln	ν SiO
						939	938	939	936	936	936	936	936	936	Kln	δ AlOHAl
915	915	919	913	919	914	913	913	914	914	914	914	915	915	915	Ill, Kln, Glc	δ AlOHAl
876		876													Cal	ν_2 CO_3
		824		827											Glc	δ Fe^{2+}OHFe^{3+}
836	835		834		833	832	830								Ill	δ AlOHMg
798			795		795	790	793	792							Ill	δ Al–O–Al
776																
751	750	751		751	751	751	752	752	752	752	753	754	754	754	Ill, Kln, Glc	δ Al–O–Si, Si–O
712		711		711											Cal	ν_4 CO_3
697	693		697		696	698	697	698							Ill	δ Si–O
668		668		668				664							Glc	δ Si–O, Fe–O
									675	675	675	672	674	674	Bhm	ν_3 Al–O
							650		648	647	649	648	648	648	Bhm	ν_3 Al–O
						536	537	537	539	538	537	538	538	538	Kln	δ Si–O–Al
			532		532										Ill	δ_3 Si–O–Si
524	523														Ill-Fe	δ_3 Si–O–Si
		517		517											Glc	δ_2 Si–O–Si
471	471	467	471	467	471	472	471	471	472	473	474	474	474	474	Ill, Kln	δ_1 Si–O–Si δ Si–O–Al

there are no geochemical data available for these tuffs (Šćavničar and Nikler, 1976; Velić et al., 1994, 2002, Pellenard et al., 2013; Picotti and Cobianchi, 2017). One of potential possibilities is that the plagioclases, if they were present in the parent material, led to the formation of the negative europium anomaly upon their dissolution during bauxitisation, which has been proposed as one of such mechanisms in Badamlu bauxite deposit (Abedini et al., 2020a,b).

5.2. *Genesis of Rovinj-1 bauxite*

The Rovinj bauxite has a predominantly uniform chemical (Fig. 12) and mineralogical composition (Fig. 8). Most trace elements also display a uniform composition along the studied bauxite profile, such as HFSE, most transitional metals (Fig. 13) and HREE (Fig. 14C and D). These elements were accumulated and enriched during bauxitisation, while LILE, K_2O, MgO and MnO were leached and depleted, which is based on their UCC normalised values. This is commonly observed in bauxites elsewhere, as immobile elements such as HFSE and REE are retained during bauxitisation (Mongelli, 1997; Calagari and Abedini, 2007; Abedini and Calagari, 2014; Mongelli et al., 2014; Ellahi et al., 2017; Abedini et al., 2020a,b) while more mobile elements such as bases and LILE are leached away (Mongelli, 1997; Calagari and Abedini, 2007; Xiao et al., 2021). This is also supported through multivariate statistical analysis, as these two groups are also separated on the PCA plot (Fig. 18), as well as in the correlation matrix where they are mutually correlated within their respective group (Fig. 17). HFSE, HREE and most transitional elements are also correlated and grouped with TiO_2 and Al_2O_3 (Figs. 17 and 18), indicating their association with boehmite, kaolinite and titanium oxides. The high kaolinite (Fig. 8) and SiO_2 (Fig. 12) content of the bauxite and a generally planar morphology of the deposit (Fig. 3) suggest of the close position of the bauxite to the water table (Bardossy, 1982; Combes and Bardossy, 1995), which prevented deeper karstification and reduced the efficiency of drainage necessary for the removal of bases and silica (Bardossy, 1982). The fact that the

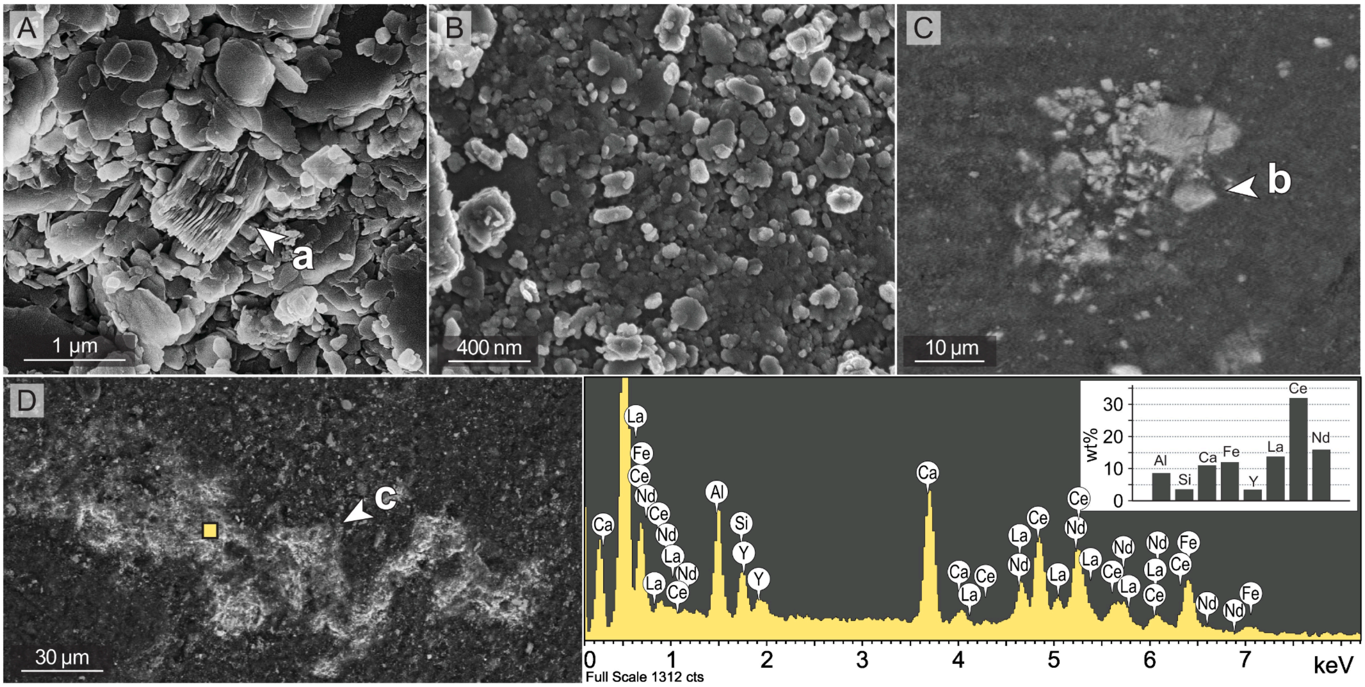

Fig. 11. SEM photomicrographs of the samples. (A) vermiform-like kaolinite crystals (a). (B) Kaolinite nanoparticles. (C) Authigenic ilmenite (b). (D) Vein of authigenic LREE-bearing mineral (c). (E) EDS spectra and semiquantitative composition of the LREE-bearing mineral.

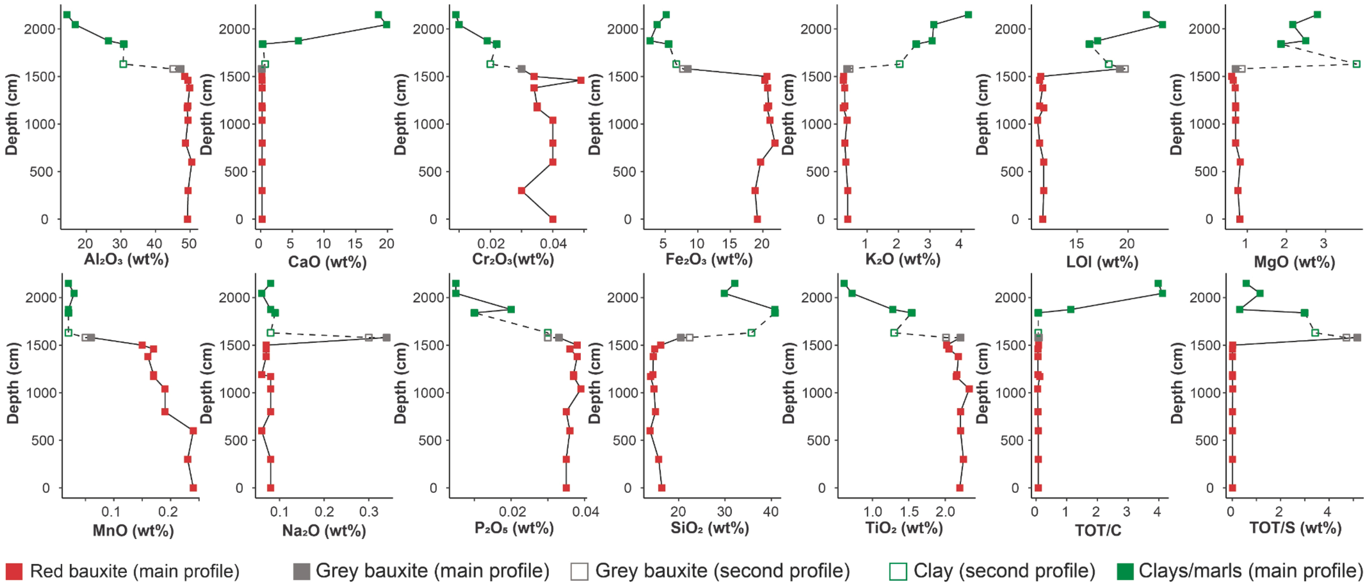

Fig. 12. Major oxide compositions recorded along the main profile (connected with solid black line), with the addition of grey bauxite and clay sample from the second profile (connected to the main profile values with black dashed line).

bauxite contains only boehmite is indicative of its formation in a karstic environment, since boehmite has been proven to form instead of gibbsite in mildly alkaline solutions (Papée et al., 1958, as cited by Bardossy, 1982) and in the presence of HCO_3^- ions (Schellmann, 1964a, cited by Bardossy, 1982). The predominantly geochemical and mineralogical composition of the deposit indicates that it formed primarily in situ (cf. Bardossy, 1982; D'Argenio and Mindszenty, 1992), but the presence of clastic bauxite lithologies in the upper parts of the deposit indicates bauxite reworking, and a possible input of different bauxite material from neighbouring bauxite deposits, suggesting that at least a part of the bauxite is parautochthonous in origin.

The tropical vegetation cover is one of the factors that promotes bauxitisation, as it generates acidic solutions via the production of organic acids and carbonic acid through the decomposition of organic matter (Gardner, 1970; Lucas, 2001). This promotes the removal of bases from the bauxite and increases the mobility of Fe and Al as they are more soluble under acidic conditions (Bardossy, 1982 and references therein; Lucas, 2001; De Campos et al., 2023). The vegetation cover also serves as a protection from erosion by torrential rainflows (Bardossy, 1982 and references therein), which was present during the formation of the Rovinj-1 bauxite, as the major parts of the bauxite are mainly pelitomorphic to microclastic, without any major indicators of erosional disturbance (Fig. 4). However, this was not always the case, as in the upper section of the bauxite the structure is predominantly clastic, with

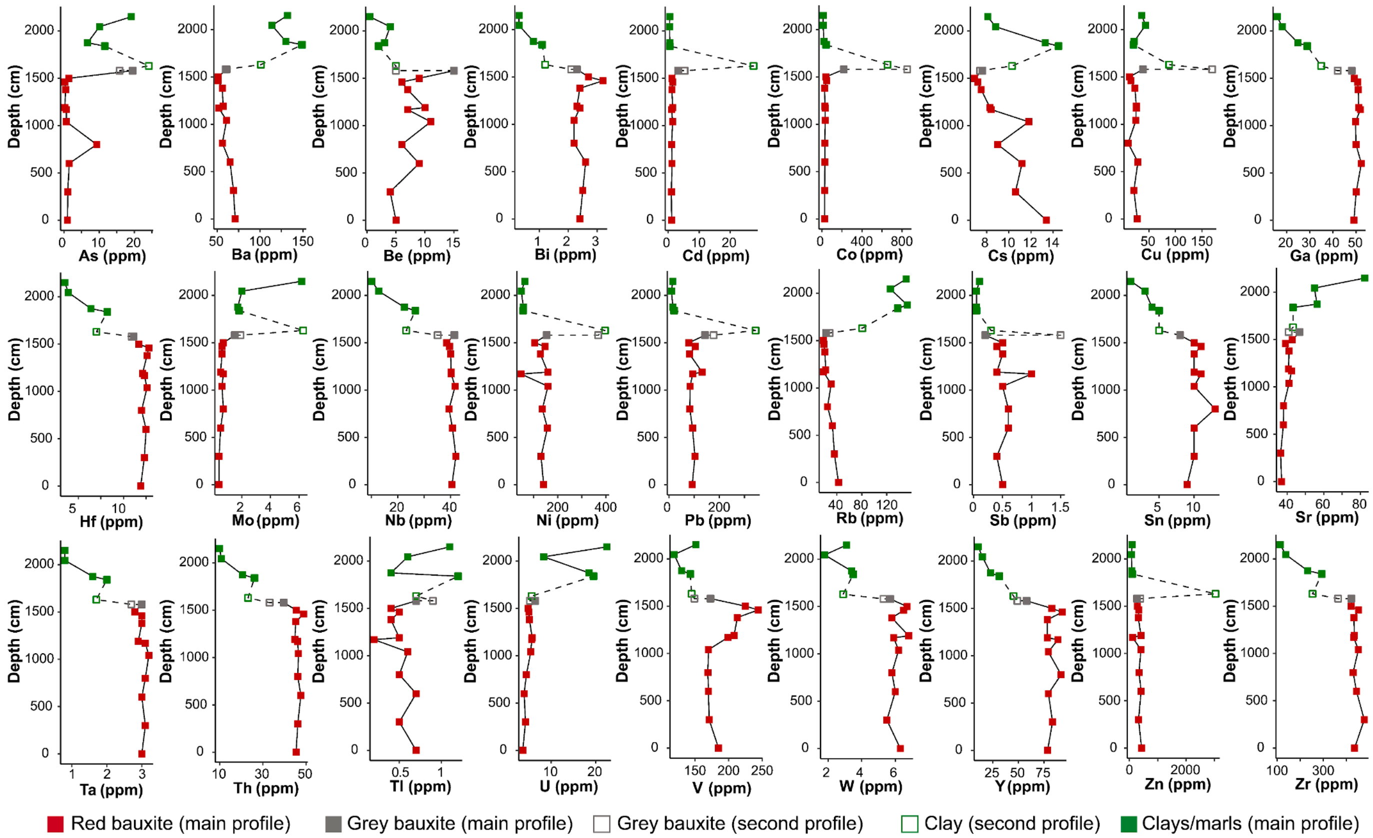

Fig. 13. Trace element compositions recorded along the main profile (connected with solid black line), with the addition of grey bauxite and clay sample from the second profile (connected to the main profile values with black dashed line).

the coarsening-upward trend (Fig. 4), indicating an intensifying degree of erosion as a result of the diminishing vegetation cover. The bauxite grains in these clastic lithologies are also enriched in iron oxides compared to the bauxite matrix (Fig. 5D, E), while also being accompanied by reworked iron oxide impregnations, in situ iron oxide impregnations and iron-rich pseudooids (Fig. 5D, E, F). These iron accumulation features are altogether indicative of climate aridification, since the longer dry season during bauxitisation leads to the formation of ferricretes in karstic bauxites (Bardossy, 1982 and references therein) and precipitation of iron-rich grain coatings (Yang et al., 2019). The climate aridification is recorded in NW Europe during the Tithonian (Wignall and Ruffell, 1990; Hesselbo et al., 2009; Yang et al., 2019; Błażejowski et al., 2023), which temporally coincides with the end of bauxite deposition, since the cover of the deposit is of upper Tithonian age. The increasing erosion can be linked to the prolonged annual dry seasons which negatively impacted the vegetation cover, leading to its reduction and increased bauxite erosion. Lower Cretaceous bauxites from the Villeveyrac basin experienced a similar evolution, where the progressive coarsening upward in the bauxite was linked to the aridification in the palaeoclimate, which led to an increase in erosion towards the end of its formation (Chanvry et al., 2020).

The upper part of the Rovinj-1 bauxite also exhibits a higher Fe_2O_3 content which supports the aforementioned petrographic observations. This increase in Fe_2O_3 is also coupled with an increase in Be, Cd, P_2O_5, S, Sr, U, Mo and W. This is not surprising as iron oxides commonly adsorb most of these trace elements such as U (Newsome et al., 2015; Scott et al., 2017; Bower et al., 2019), P (Weng et al., 2012), Mo (Goldberg et al., 1996), S (Parfitt and Smart, 1978) and Cd (Shen et al., 2020). Although V does not show a strong statistical affiliation with iron oxides (Figs. 17 and 18), it is clearly enriched in the upper section of the bauxite (Fig. 13), where it may be linked to the observed increase in the Fe_2O_3 content (Fig. 12) and iron impregnations. The bases and LILE display the opposite trend, as their content is increasing towards the bottom of the bauxite (Figs. 12 and 13), which is linked to the increasing alkalinity in the lower sections of the bauxite, close to the carbonate bedrock, where a similar process was reported in several other studies (Maksimović et al., 1991; Mongelli, 1997).

5.3. *Behaviour of REE in the Rovinj-1 deposit*

LREE and MREE do not show any close statistical association with other trace and major elements, suggesting their mobility during bauxitisation (Figs. 17 and 18), which can also be seen from their enrichment or depletion throughout the studied bauxite profile (Fig. 14C and D), best visible through the variations in the $(La/Yb)_{ch}$ and $(Gd/Yb)_{ch}$ ratios (Fig. 15). The LREE and MREE enrichment is present only in the upper section of the bauxite profile, where it is commonly accompanied with the negative Ce anomaly (Figs. 14C, D and 15). The topmost section of bauxites in general is usually more leached than the rest of the bauxite body, which consequently leads to the development of a positive Ce anomaly (Mongelli, 1997; Wang et al., 2013; Vind et al., 2018, Ahmadnejad and Mongelli, 2022), as Ce is retained in its oxidised form and the rest of the REE are leached downwards. This leads to the depletion of Ce in the percolating fluids compared to the other REE, facilitating the development of a negative Ce anomaly and enrichment in other REE in the lower sections of bauxites (Mongelli, 1997). The positive Ce anomaly is not visible in the topmost section of the Rovinj-1 bauxite (Figs. 14C, D and 15), as the constant reworking of the bauxite and erosion in the topmost part of the bauxite likely masked the positive Ce anomaly or removed the bauxite with such geochemical signature altogether from the studied profile. It should be noted that the positive Ce anomaly was observed in the first clay/marl layer in the cover sequence (Figs. 14E, F and 15), whose REE signature was likely partially inherited from the bauxite, since it formed directly on top of the grey

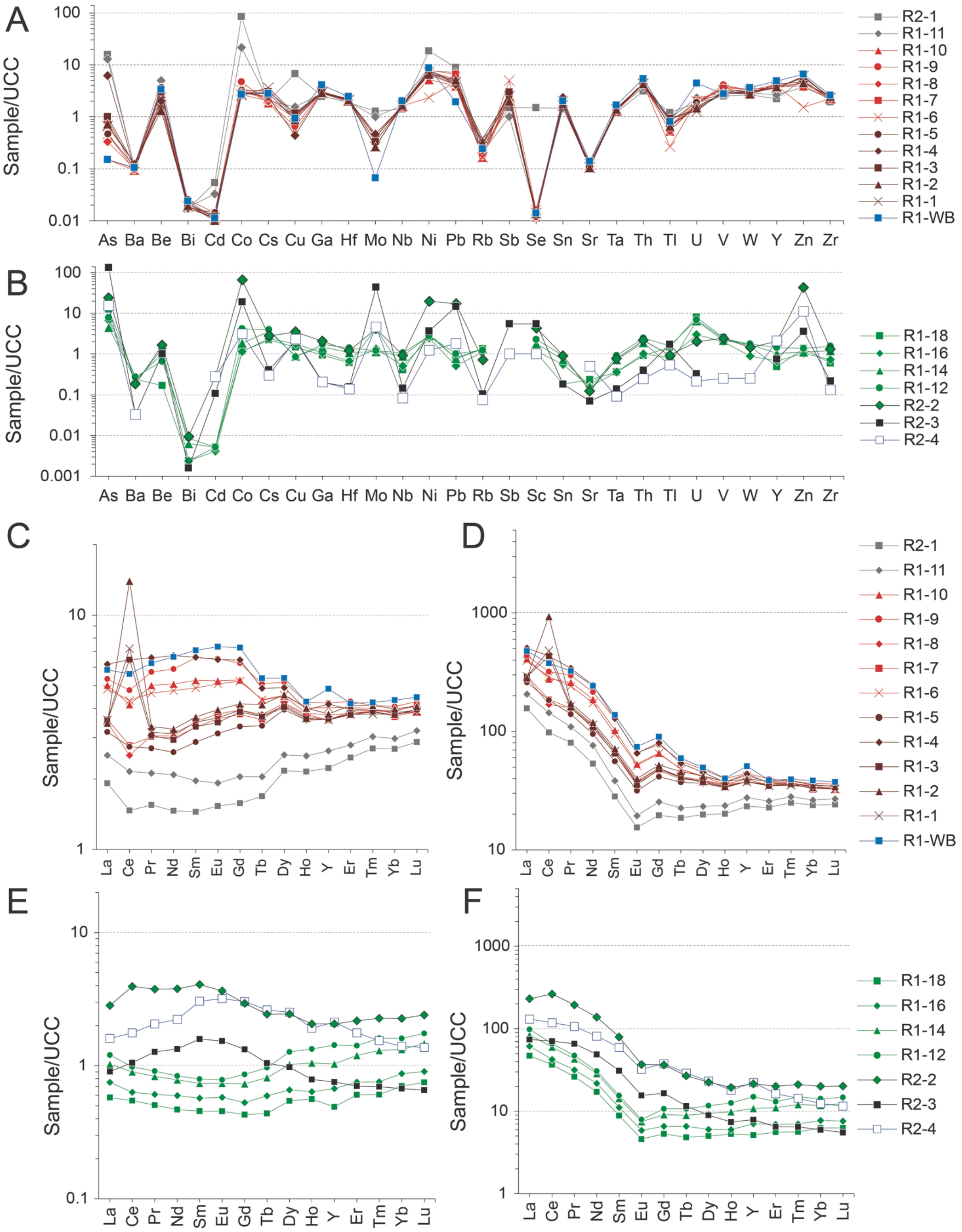

Fig. 14. Trace and rare earth element values after their normalisation using the Upper Continental Crust Values (UCC) and chondrite values, after Taylor and McLennan (1989). (A) Trace elements in grey, red and white bauxite samples normalised to UCC. (B) Trace elements in clays/marls, iron sulphide crusts and clayey limestone samples normalised to UCC. (C) Rare earth elements in grey, red and white bauxite samples normalised to UCC. (D) Rare earth elements in grey, red and white bauxite samples normalised to chondrites. (E) Rare earth elements in clays/marls, iron sulphide crusts and clayey limestone samples normalised to UCC. (F) Rare earth elements in clays/marls, iron sulphide crusts and clayey limestone samples normalised to chondrites.

bauxite (Fig. 4). Several horizons in the upper section of the bauxite are enriched in LREE and MREE compared to HREE, visible in the chondrite and UCC normalized REE patterns (Fig. 14C and D) and variations in (La/Yb)$_{ch}$ and (Gd/Yb)$_{ch}$ ratios (Fig. 15), which altogether indicates repeated leaching and accumulation of LREE and MREE. This apparent mobility of LREE and MREE compared to HREE is quite peculiar, since HREE are usually more easily leached than LREE in bauxites (Ahmadnejad and Mongelli, 2022), as they are more stable and soluble in their ionic form in aqueous solutions while also forming more stable LnCO$_3^+$ complexes compared to LREE (Coppin et al., 2002; Duncan and Shaw, 2003; Liankai et al., 2020). One of the possible explanations for this fractionation within the REE group could be the preferential scavenging of LREE by iron oxides (Rankin and Childs, 1976; Bau, 1999; Laveuf et al., 2008, 2012) and the increased complexation of LREE and MREE with organic acids compared to HREE (Elders et al., 1979; Lin et al., 2017; Dia et al., 2000; Cao et al., 2001; Abedini and Khosravi 2023), as both the accumulation of iron oxides and percolation of organic acids took place during bauxitisation. A similar enrichment in LREE was observed in iron- and organic-matter rich bauxite horizons in the Iranian Dopolan bauxite deposit (Ellahi et al., 2015). The HREE have constant values in the bauxite (Figs. 14C, D and 15), indicating that they were immobile and virtually unaffected by these processes. No HREE-

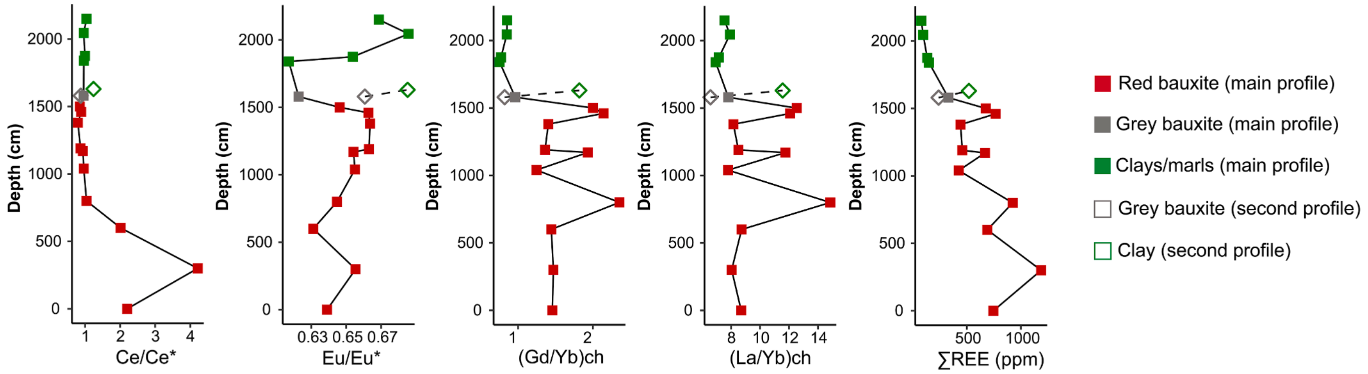

Fig. 15. Composition of different REE ratios and total REE content recorded along the main profile (connected with solid black line), with the addition of grey bauxite and clay sample from the second profile (connected to the main profile values with black dashed line).

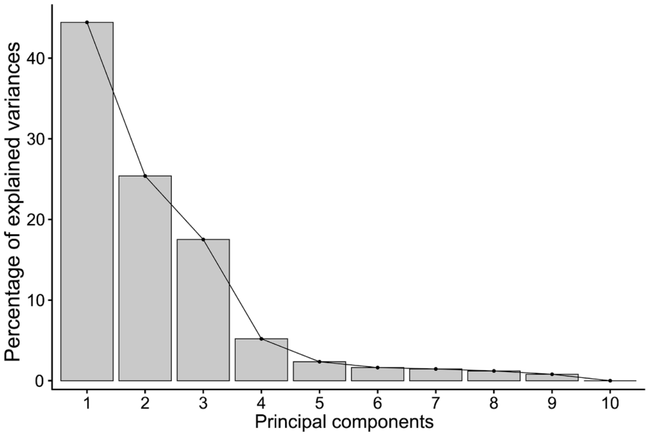

Fig. 16. Scree plot showing the proportion of variance accounted for by the individual principal components.

bearing minerals were found during the SEM-EDS analysis of selected bauxite samples, indicating that they were likely immobilised through the adsorption onto present clay minerals, which is based on the examples of HREE accumulation in kaolinitic clays during weathering (Xu et al., 2017; Borst et al., 2020). Despite the absence of HREE-bearing minerals, one type of LREE-bearing mineral was found, likely of the bastnaesite group (Fig. 11D, E), but only in the lowermost sample from the main profile (R1-1). This indicates the formation of authigenic fluorocarbonate REE-bearing minerals near the carbonate footwall in the Rovinj-1 deposit, which is a phenomenon observed in karst bauxites worldwide, responsible for positive Ce anomalies near the footwall (Maksimović et al., 1991; Mongelli, 1997; Mongelli et al., 2021; Abedini and Khosravi 2024). This, however, cannot fully explain the observed highly positive Ce anomalies and depletion in other REE in the lower section of the bauxite (Fig. 14C and D), since this mineral was found only near the footwall and is also enriched in the rest of LREE (Fig. 11E). This means that there should be also an enrichment in LREE in the lower section of the bauxite with a weak or absent Ce anomaly, and not the high positive Ce anomaly with LREE depletion which was observed. This means that Ce was likely enriched via other processes, likely through leaching of other REE and immobilisation of Ce through its oxidation from Ce^{3+} to Ce^{4+} in the presence of ferromanganese oxides (Kawabe et al., 1999; Ohta and Kawabe, 2001; Quinn et al., 2006). Usually, this results in the precipitation of cerianite (Braun et al., 1998; Bau, 1999; Dia et al., 2000, Ahmadnejad and Mongelli, 2022), but since no presence of such mineral was found, it is likely that Ce was retained through the adsorption into ferromanganese oxides (Koppi et al., 1996; Coelho and Vidal-Torrado, 2000; Neaman et al., 2004). Therefore, the lower section of the bauxite was likely forming for a prolonged period of time before the upper section of the bauxite was deposited, which allowed these processes to take place. The mainly pelitomorphic structure of the lower bauxite section also supports this (Fig. 4), indicating that it was formed during more stable conditions compared to the upper section which experienced multiple depositional and redepositional cycles. This should be confirmed by future studies with much more detailed SEM-EDS analysis and sample set, as it is possible that some other REE- and Ce-bearing minerals were missed due to a relatively small number of analysed samples with SEM-EDS.

5.4. *Beginning of the transgression*

The sea-level rise and flooding of the previously emerged areas followed the formation of Rovinj-1 bauxite, which led to multiple epigenetic changes in the deposit, most notable being the processes of pyritisation and epigenetic resilicification. The bauxite experienced resilicification in its upper and lower parts, as indicated by the higher kaolinite (Fig. 8) and SiO_2 content in the grey bauxite (Fig. 12), in situ growth of kaolinite (Fig. 5J; cf. Mameli et al., 2007; Mongelli et al., 2021), and the presence of bauxitic clay in the contact zone between the bauxite and the bedrock (pers. comm. Milan Mihovilović). Pyritisation affected the uppermost section of the bauxite, producing a half-metre-thick zone of grey bauxite with abundant pyritised roots and pyrite impregnations (Figs. 4 and 5K, L), which is linked to microbial reduction in the presence of organic matter and the solubilised iron in the marshy environment (Berner, 1970). The marshy environment was established atop of the Rovinj-1 bauxite during its flooding, which is a commonly observed phenomenon in karst bauxites (Bardossy, 1982; Šinkovec et al., 1994; Laskou and Economou-Eliopoulos, 2007, 2013; Economou-Eliopoulos et al., 2022). White bauxite also formed in this phase, mainly along the fractures and pyritised roots (Fig. 4), which happened as the acidic and reducing porewaters percolated along the fractures into the bauxite. Part of the white bauxite formed through the microbial decomposition of roots, since a similar process was observed in one of the bauxite bodies of the Parnassos–Ghiona deposits (Kalaitzidis et al., 2010). Most of hydrogen sulphide produced was likely immediately precipitated upon contact with solubilised iron in the grey bauxite zone, and as such, the percolating porewaters devoid of hydrogen sulphide, but still depleted in oxygen, only solubilised the iron oxides without the formation of iron sulphides, leaving behind the deferrified white bauxite. The removal of iron oxides also affected the trace elemental signature, as it is depleted in Mo, Pb and As as compared to the red bauxite (Fig. 15A), which are commonly hosted within iron oxides (Bowell, 1994; Goldberg et al., 1996; Shen et al., 2020). There is also a slight U enrichment (Fig. 15A), which might be linked to its immobilisation by the reducing porewaters (Newsome et al., 2015; Scott et al., 2017; Bower et al., 2019). White bauxite is also enriched in LREE and MREE

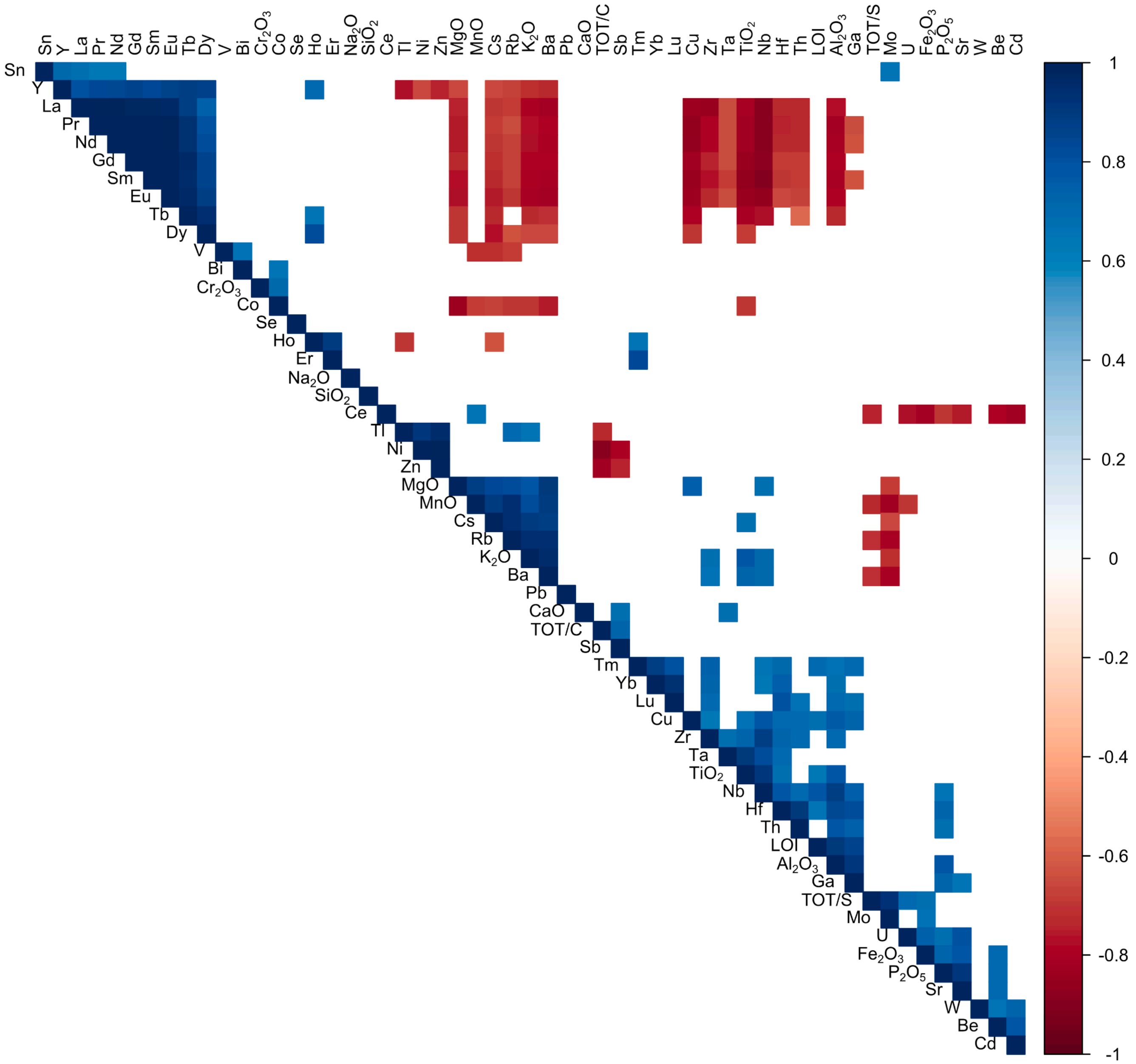

Fig. 17. Constructed correlation matrix for major, trace and rare earth elements in the red bauxite samples. Blank cells represent statistically insignificant values.

(Fig. 15C), which were either inherited from the original red bauxite during its reduction, or were delivered by the percolating fluids which likely contained organic acids which enrich and more easily form complexes with LREE and MREE compared to HREE (Elders et al., 1979; Lin et al., 2017; Dia et al., 2000; Cao et al., 2001). The formation of the grey and white bauxite was followed by the formation of the first clay layer (R2-2), which is accompanied by clayey limestone lenses with iron sulphide crusts (Fig. 4). This clay most likely formed through reworking and resilicification of the topmost bauxite in the marshy environment. This is supported by the presence of the positive Ce anomaly (Fig. 14C and D), which had to be inherited from the ferralitic material as it could not have been developed in the reducing environment. The REE signature also displays a LREE and MREE enrichment compared to the other clays/marls (Fig. 15D), which could have been inherited from the bauxite. This enrichment could have been formed through the liberation of LREE and MREE from iron oxides during the reduction of red bauxite and their interaction with organic matter. This is a possible scenario, since both the clayey limestone lenses and iron sulphide crusts display the same LREE and MREE enrichment (Fig. 15D), indicating that the environment in which these materials formed likely exhibited such REE signature. The first clay layer also contains similar amounts of almost all trace elements as the grey bauxite below it (Fig. 13), which likewise supports the formation of this clay from the bauxite. This clay is also enriched in As, Mo, Pb and Zn compared to the grey bauxite (Fig. 13), which was linked to their accumulation in an euxinic environment during pyrite formation (Fig. 19). The abundance of these elements in the first clay layer compared to other clays/marls in the cover sequence is likely not only a consequence of redox conditions, but also of the increased supply of these elements during the initial flooding of the bauxite, as bauxite already has a high content of most trace elements (Fig. 13), some of which were likely released and sequestrated during its reduction.

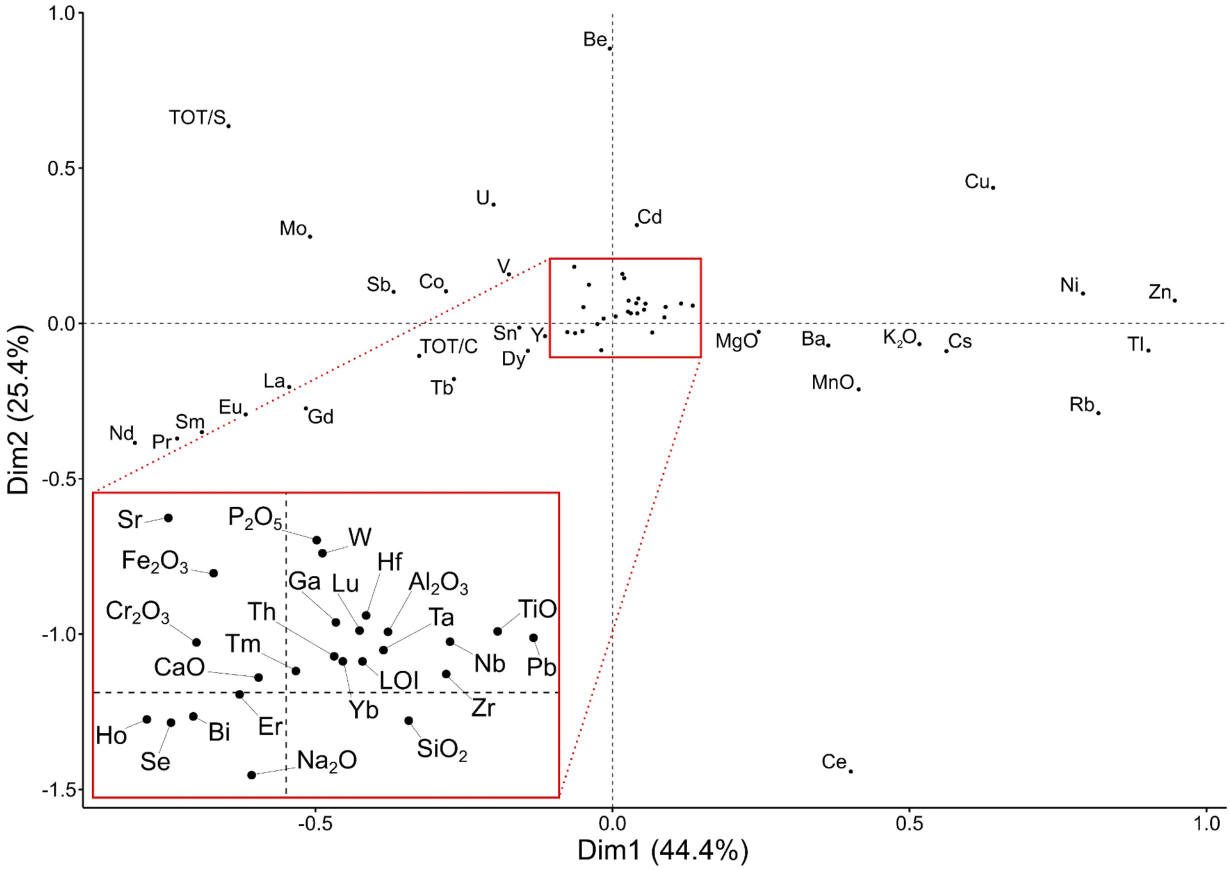

Fig. 18. PCA plot showing the relationships between major, trace and rare earth elements in the red bauxite.

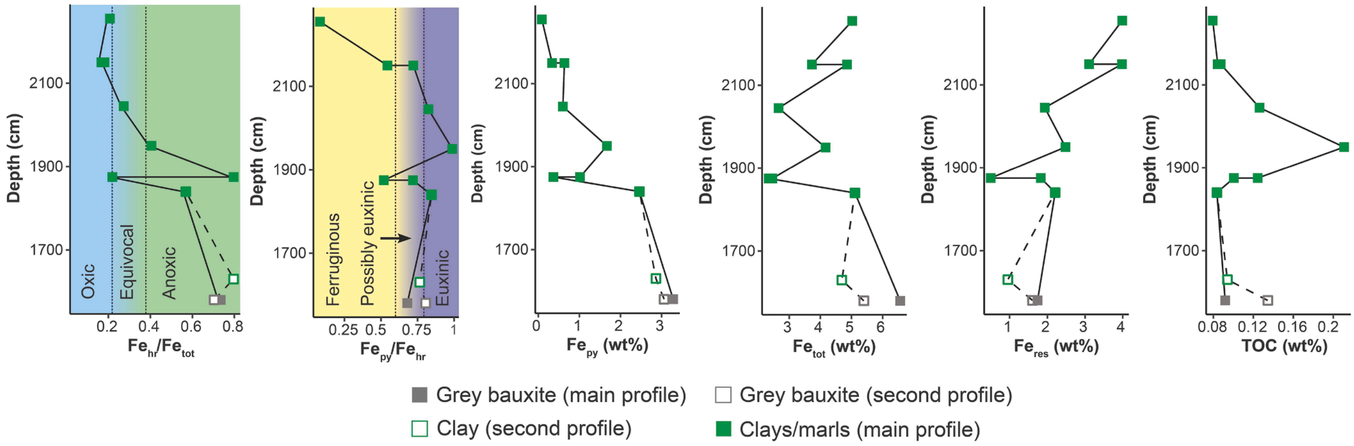

Fig. 19. Plots of Fe_{hr}/Fe_{tot}, Fe_{py}/Fe_{hr}, Fe_{py}, Fe_{tot}, Fe_{res} and TOC values recorded from clays/marls and grey bauxite along the main (connect with solid black line) and second profile (connected to the main profile values with black dashed line).

5.5. *Cover sequence*

5.5.1. *Palaeoclimatic evolution*

The alternating sequence of clays/marls, limestones and black-pebble breccias followed the deposition of the first clay layer (Fig. 4). The cyclical character of this sequence is likely a consequence of the sea-level oscillations as the transgression progressed. The clays/marls from the cover sequence are composed of same minerals as the first clay layer, but they display a gradual increase in MLIS and illite, coupled with the decrease in kaolinite content (Figs. 8 and 10). This is also visible in the major oxide content, through the decrease in Al_2O_3 and increase in K_2O content (Fig. 12). This trend is probably linked to the progressive climate aridification in the latest Tithonian, which began during the end of bauxite deposition, and continued during the deposition of the bauxite cover sequence. Several studies in NW Europe recorded similar changes in clay mineralogy during Tithonian, which was linked to climate aridification (Wignall and Ruffell, 1990; Hesselbo et al., 2009; Błażejowski et al., 2023). During the existence of the karstic lake which formed atop of the bauxite, portions of surrounding areas were most likely still emerged, where pedogenesis was likely still an ongoing process. As such, the soils forming on these emerged areas could have responded to climate aridification with the increased bisialitisation (formation of 2:1 clay minerals) and the reduction in sialitisation (formation of 1:1 clay minerals), producing a progressively more illitic depositional sequence. This is also visible in trace element composition of the clays/marls, as there is a gradual decrease in HFSE content (Fig. 13), which accumulate during the processes of ferralitisation, and as such, the reduction in the production of ferralitic soils could have impacted the HFSE content of the developing clays/marls. Such newly formed soil materials were washed into the lake and reworked into the clays/marls that are preserved in the cover sequence of the Rovinj-1 bauxite. The clays/marls have the same REE signature which differs from the first clay layer, as they display a clear depletion in LREE and an enrichment in HREE (Fig. 14E and F), visible also in their differences in $(La/Yb)_{ch}$ and $(Gd/Yb)_{ch}$ ratios (Fig. 15). HREE are generally more soluble than LREE in aqueous environments, since they form more stable carbonate and aqueous complexes (Coppin et al., 2002; Duncan and Shaw, 2003; Liankai et al., 2020), which likely led to their increased adsorption onto present clay minerals compared to LREE. The increased adsorption of HREE onto clay minerals compared to LREE in saline solutions (Coppin et al., 2002; Hao et al., 2019) might have also played a part in the formation.

5.5.1.1. Palaeoenvironmental evolution. The limestones in the cover sequence are mainly bioclastic to peloidal wackestones but bioclastic to peloidal packstones are also present (Fig. 7A, B). Sporadic occurrences of fenestrae (Fig. 7B) indicate local ephemeral exposure during the evolution of the karstic lake. The abundance of pellets (Fig. 7A) and laminar textures (Fig. 7E) suggest sedimentation in a low-energy environment, which is expected in an isolated karstic lake. The faunal record in the limestones from this sequence is dominated by ostracods and *Charophyta* oogoniums, with sporadic occurrences of miliolid foraminifera and *Favreina* pellets (Fig. 7A, B, C), indicating the formation in a restricted schizohaline karstic lake. The presence of glauconite in the upper section of the cover sequence is an indicator of marine influence, as its formation requires the source of potassium (Odin and Matter, 1981; Giresse and Wiewióra, 2001; Meunier and El Albani, 2007; Baldermann et al., 2015, 2017), which is readily found in the seawater. Another glauconite occurrence was found in the contemporaneous palaeosol nearby (Perković et al., 2024), which indicates that this glauconitisation event was widespread during the late Tithonian transgression in this area. The deposition of the cover sequence ends with the deposition of the fully marine Kirmenjak limestone over the bauxite cover sequence (Figs. 2 and 3), which indicates the overland transgression of the surrounding terrain and the complete ingression of the former karstic lake. A similar sequence was described in one of the blue holes in the Bahamas (Rasmussen and Neumann, 1988). There, a depositional sequence was observed which starts with karstification and palaeosol formation, which is followed by the deposition of limestones in a schizohaline environment, and finally fully marine limestone. Such blue hole sequence is typical for the “internal transgression” (Rasmussen and Neumann, 1988), in which the internal water table rises through karstic conduits in the palaeotopographic depressions during the initial stage of the transgression before the emerged terrain completely drowns. Similar blue hole sequence was also described in the cover of the Hungarian Gánt bauxite deposit (Bignot et al., 1985; Trabelsi et al., 2021).

5.5.1.2. Redox evolution. The iron speciation data, mineralogy and geochemistry of the clays/marls from the cover sequence of the Rovinj-1 bauxite mainly support the blue hole model, while providing additional insight into the evolution of the palaeoenvironment of the isolated karstic lake. During the first stages of the transgression, the karstic lake was characterised by euxinic bottom waters, which is indicated by iron speciation data (Fig. 19), abundance of pyrite (Fig. 19) and elevated content of chalcophile elements in the first clay layer and the grey bauxite (Figs. 12 and 13). As the transgression progressed, the redox conditions progressively shifted towards equivocal, and finally oxic (Fig. 19). This shift is coupled with the decrease in Fe_{py} content (Fig. 19), TOT/S content (Fig. 12), and the appearance of glauconite (Table 1), which support this shift in redox conditions. The residual iron content also increased (Fig. 19), which indicates that most of the iron in the upper part of the cover sequence is present in glauconite and illite and not in iron sulphides. The redox sensitive elements such as Mo, U and V together with some chalcophile elements such as As and Tl (Fig. 13) display an enrichment in the top part of the cover sequence, which contrasts with the iron speciation and mineralogical data, as the accumulation of these elements usually happens in anoxic and euxinic conditions (Wanty and Goldhaber, 1992; Goldberg et al., 1996; Shaheen et al., 2016; Bower et al., 2019; Fuller et al., 2020). A similar trend was observed in the succession of the Spanish La Pedrera de Meià karstic lake (Gil-Delgado et al., 2023), where the values of chalcophile and redox-sensitive elements increase towards the top of the succession, coinciding with the expansion of the lake during its complete flooding. Gil-Delgado et al. (2023) proposed that this led to the renewed supply of these elements into the lake and the increase of biologically-derived particulates carrying these elements, which altogether boosted their accumulation. A similar scenario could be proposed for the cover sequence of the Rovinj-1 bauxite deposit, as it experienced a similar evolution during the transgression. The change in redox conditions from euxinic towards oxic (Fig. 19) in the cover sequence of the Rovinj-1 bauxite deposit is most likely the result of several factors, one of them being the increase in sea-level rise, which led to the connection of this karstic lake with the nearby marine environments and possibly better circulation in the lake, which decreased the redox stratification in the lake. One of the other factors could be the change in the supply of organic matter, whose accumulation and microbial decomposition likely had a big influence on the development of anoxic and euxinic conditions in the lake, since the microbially facilitated decomposition of organic matter removes oxygen, producing anoxic conditions (Berner, 1970). It should be noted that there is practically no preserved organic matter in the clays/marls as they have a very low TOC content (Fig. 19), indicating that virtually no organic matter was preserved in the sediment because it was consumed during microbial activity. One of the possible causes for the changes in the supply of organic matter could have been the aridification of climate which begun during the end of bauxite deposition and continued during the deposition of the cover sequence, as aridification can cause the decrease in plant productivity (Hu et al., 2021), leading to diminished supply of plant organic matter. The progressive sea level rise could have also impacted the supply of plant organic matter, through the gradual flooding of the surrounding emerged areas, leading to the reduction of terrestrial plant habitats. Flooding episodes of coastal regions can also cause the accumulation and mineralisation of organic matter in soils (Sahrawat, 2003), but in some cases also can lead to increased mobilisation of solubilised organic matter, increasing its supply into the seawater (Majidzadeh et al., 2017). Based on the above processes and observations, we tentatively suggest that the combined influence of the progressive sea-level rise and the changes in the supply of organic matter were a possible cause of the observed redox conditions during the evolution of the karstic lake, but future detailed studies with improved methodology could provide a better understanding of the factors that impacted the redox evolution within the lake.

6. Conclusions

This study focused on the genesis of the Rovinj-1 bauxite deposit situated in the Istrian part of the Adriatic Carbonate Platform (AdCP) and the associated changes in its surrounding environments and climate during its formation within the Late Jurassic subaerial exposure phase. This study also focused on the behaviour of REE and trace elements during bauxitisation, which were also used as proxies for the physicochemical changes that influenced the formation of the Rovinj-1 bauxite deposit and its cover sequence. The study of the cover sequence was additionally complemented by the use of iron speciation data to enable a more detailed reconstruction of the redox changes that followed the flooding of the bauxite. Based on the data collected, several important conclusions can be drawn, as follows:

1. The formation of the Rovinj-1 bauxite is polygenetic and was enabled by the uplift of the NW part of the AdCP in response to the obduction of the Vardar Ocean ophiolites in the Late Jurassic, after which the karstification processes and the bauxitisation of the accumulating volcanic ash, aeolian dust and insoluble residue of the carbonate bedrock took place (Fig. 20A).
2. The chemical and mineralogical uniformity of the Rovinj-1 bauxite suggests primarily in situ formation, although the clastic bauxite lithologies indicate some reworking and possible local input, especially during the latest stage of its formation, related to the progressive regional aridification in the late Tithonian which led to

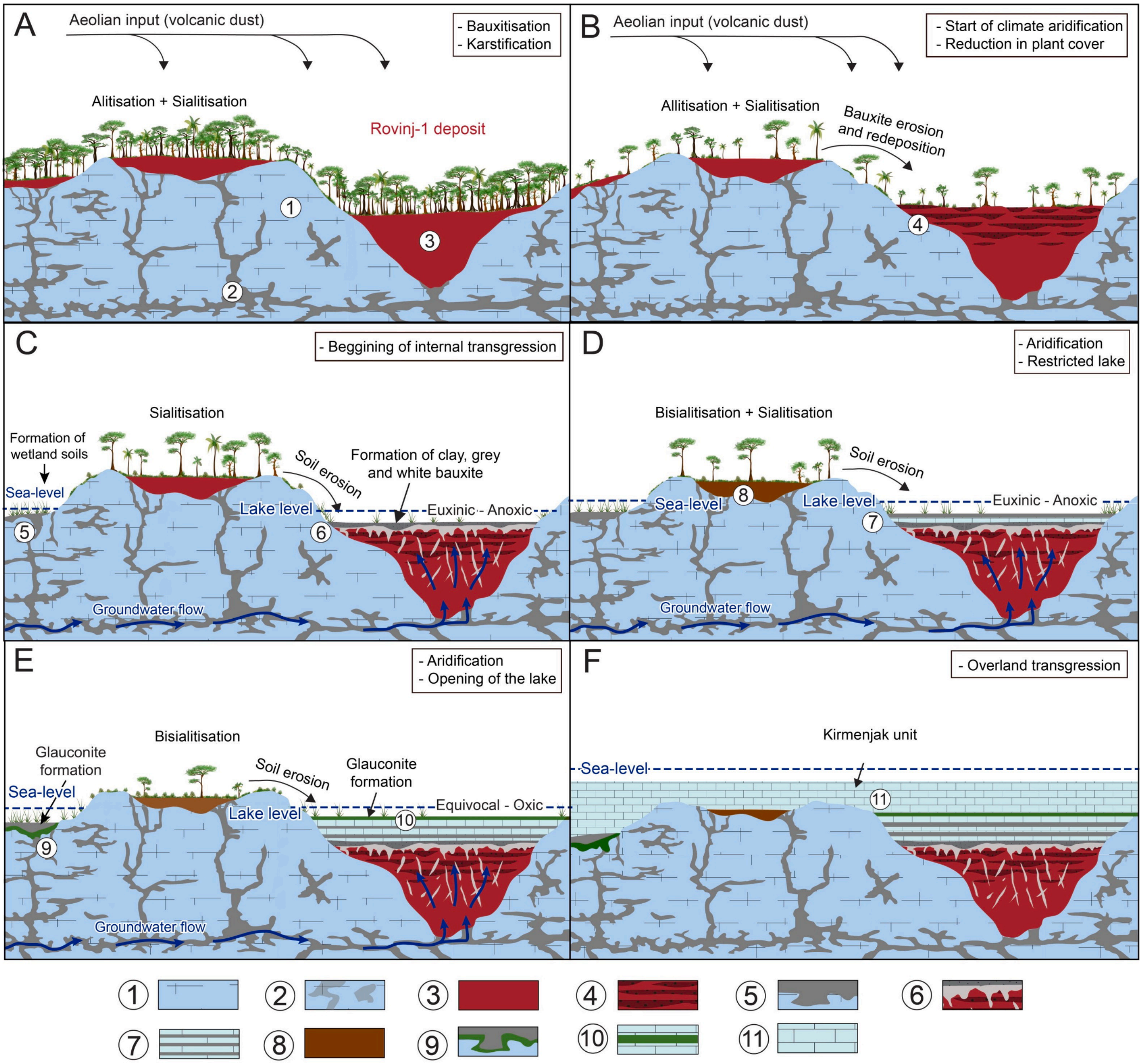

Fig. 20. Summarised genesis of the Rovinj-1 bauxite deposit and its surrounding area. (A) Karstification of emerged carbonates and bauxitisation of aeolian and volcanic dust together with insoluble carbonate residue. (B) Start of the climate aridification which led to the reduction of plant cover, allowing the increased erosion and redeposition of Rovinj-1 bauxite and surrounding soils and bauxites. (C) Beginning of transgression started as an internal transgression which led to the formation of karstic lake above the Rovinj-1 bauxite comprising grey and white bauxite together with clays formed under euxinic to anoxic conditions. (D) Continued climate aridification recorded through increasing illite and mixed-layered illite–smectite and reduction in kaolinite content in clays/marls deposited together with limestones under anoxic to euxinic conditions. (E) Continued climate aridification indicated by further decrease in kaolinite content and increase in illite and mixed-layer illite–smectite in clays/marls deposited together with limestones under equivocal to oxic conditions as the lake was progressively more connected with surrounding sea as also indicated by the local glauconitisation in Rovinj-1 deposit and Zlatni rt palaeosol (Perković et al., 2024). (F) End of subaerial exposure phase – overland transgression of the emerged carbonate terrain and deposition of shallow-marine Kirmenjak unit. Legend: 1 – Ofxordian to lower Kimmeridgian Muča unit; 2 – karstification, 3 – bauxite and ferralsols; 4 – clastic bauxite; 5 – wetland soils; 6 – grey and white bauxite; 7 – alternation of clays/marls and limestones; 8 – soils hosting bisialitisation and sialitisation; 9 – glauconite in clays/marls; 10 – glauconite in palaeosols; 11 – limestones of upper Tithonian Kirmenjak unit.

the decrease in the vegetation cover and increased erosion of the bauxite and its surroundings (Fig. 20B).

3. REEs and trace elements also indicated the physicochemical changes during the formation of the bauxite, highlighting the differences between the lower and the upper part of the bauxite, which was subjected to increased erosion and the formation of iron oxide impregnations and iron-rich bauxite. Positive and negative Ce anomalies indicated the changes between the formation of the lower and upper parts of the bauxite, suggesting that bauxite formation occurred in two phases. The $(La/Yb)_{ch}$ and $(Gd/Yb)_{ch}$ ratios, as well as UCC and chondrite normalized REE values, also showed the fractionation between LREE, MREE and HREE, where HREE were mainly immobile during bauxitisation, while LREE and MREE were mobile and affected by the behaviour of organic acids and iron oxides.
4. Progressive aridification continued during the formation of the bauxite cover sequence, as recorded by the changes in clay mineral composition due to the increased formation of illite and MLIS over kaolinite (Fig. 20C).
5. The initial flooding of the bauxite led to the formation of pyrite-rich grey bauxite and development of white deferrified bauxite (Fig. 20D). The sea-level rise begun as an oscillating internal transgression progressing into the overland transgression, with the increasing salinity of the lake being recorded through the occurrence of glauconite in the upper part of the cover sequence (Fig. 20E, F). The transition from the internal towards an overland transgression is marked by the deposition of fully marine upper Tithonian Kirmenjak limestone. Based on the aforementioned, faunal and floral assemblages as well as with structures and textures of the overlying limestones, the cover sequence of the Rovinj-1 bauxite is interpreted as the blue hole sequence.

In summary, the genesis and evolution of the Rovinj-1 bauxite deposit reflects a complex interplay of tectonic, climatic, depositional and physicochemical processes. Overall, this study provides novel insight into the genesis of the Rovinj-1 bauxite deposit and contributes to the current understanding of the late Oxfordian/early Kimmeridgian to late Tithonian subaerial exposure phase in the NW part of the AdCP. One of the most important contributions is the evidence of a climate shift towards more arid conditions in the late Tithonian, which improves the current understanding of climate changes in the Late Jurassic of the AdCP but also wider region. The detailed analysis of the bauxite cover sequence also provided additional insight into the evolution of the transgression that followed the long subaerial exposure phase and its impact on the surrounding palaeoenvironments. The detailed analysis of trace elements and REE enabled the creation of a much more detailed genetic model of the Rovinj-1 bauxite deposit and confirmed that they are an invaluable tool for the study of bauxite formation and palaeoenvironments in general.

Declaration of competing interest

The authors declare that they have no known competing financial interests or personal relationships that could have appeared to influence the work reported in this paper.

Data availability

Data will be made available on request.

Acknowledgements

This work has been fully supported by the Croatian Science Foundation under the project IP-2019-04-8054 – WIANLab (Western Istrian Anticline as an Ideal Natural Laboratory for the Study of the Regional Unconformities in Carbonate Rocks, PI Goran Durn). TH acknowledges support by the Jiangsu Distinguished Professor Award. We would like to thank the two anonymous reviewers for their useful comments which improved the quality of this manuscript.

Appendix A. Supplementary data

Supplementary data to this article can be found online at https://doi.org/10.1016/j.oregeorev.2024.106236.

References

Abedini, A., Calagari, A.A., 2014. REE geochemical characteristics of titanium-rich bauxites: the Permian Kanigorgeh horizon, NW Iran. Turk. J. Earth Sci. 23, 513–532. https://doi.org/10.3906/yer-1404-11.

Abedini, A., Khosravi, M., 2023. REE geochemical characteristics of the Huri karst-type bauxite Deposit, Irano-Himalayan Belt, Northwestern Iran. Minerals 13 (7), 926.

Abedini, A., Khosravi, M., 2024. Geochemical characteristics of aluminum-bearing iron ores: a case study from the Kolijan karst-type bauxite deposit, Northwestern Iran. Minerals 14 (2), 151.

Abedini, A., Khosravi, M., Dill, H.G., 2020a. Rare earth element geochemical characteristics of the late Permian Badamlu karst bauxite deposit, NW Iran. J. Afr. Earth Sci. 172, 103974.

Abedini, A., Calagari, A.A., Azizi, M.R., 2018. The tetrad-effect in rare earth elements distribution patterns of titanium-rich bauxites: evidence from the Kanigorgeh deposit, NW Iran. J. Geochem. Explor. 186, 129–142. https://doi.org/10.1016/j.gexplo.2017.12.007.

Abedini, A., Azizi, M.R., Calagari, A.A., 2019. Ree mobility and tetrad effects in bauxites: an example from the kanisheeteh deposit, NW iran. Acta Geodyn Geomat 16, 11–26. https://doi.org/10.13168/AGG.2019.0002.

Abedini, A., Mongelli, G., Khosravi, M., Sinisi, R., 2020b. Geochemistry and secular trends in the Middle–Late Permian karst bauxite deposits, northwestern Iran. Ore Geol. Rev. 124, 103660. https://doi.org/10.1016/j.oregeorev.2020.103660.

Ahmadnejad, F., Mongelli, G., 2022. Geology, geochemistry, and genesis of REY minerals of the late Cretaceous karst bauxite deposits, Zagros Simply Folded Belt, SW Iran: constraints on the ore-forming process. J. Geochem. Explor. 240, 107030.

Andersen, F.A., Brečević, L., 1991. Infrared spectra of amorphous and crystalline calcium carbonate. Acta Chem. Scand. 45, 1018–1024.

Baldermann, A., Warr, L.N., Letofsky-Papst, I., Mavromatis, V., 2015. Substantial iron sequestration during green-clay authigenesis in modern deep-sea sediments. Nat. Geosci. 8, 885–889. https://doi.org/10.1038/ngeo2542.

Baldermann, A., Dietzel, M., Mavromatis, V., Mittermayr, F., Warr, L.N., Wemmer, K., 2017. The role of Fe on the formation and diagenesis of interstratified glauconite-smectite and illite-smectite: a case study of Lower Cretaceous shallow-water carbonates. Chem. Geol. 453, 21–34. https://doi.org/10.1016/j.chemgeo.2017.02.008.

Bardossy, G., 1982. Karst Bauxites. Elsevier scientific Publishing Company, Amsterdam–Oxford–New York.

Bau, M., 1999. Scavenging of dissolved yttrium and rare earths by precipitating iron oxyhydroxide: experimental evidence for Ce oxidation, Y-Ho fractionation, and lanthanide tetrad effect. Geochim. Cosmochim. Acta 63, 67–77. https://doi.org/10.1016/S0016-7037(99)00014-9.

Berner, R.A., 1970. Sedimentary pyrite formation. Am. J. Sci. 268, 1–23. https://doi.org/10.2475/ajs.268.1.1.

Bignot, G., Blondeau, A., Guernet, C., Perrau, M., Poignant, A., Renard, M., Riveline, J., 1985. Age and characteristics of the Eocene transgression at Gánt (Vértes mts, Transdanubia, Hungary). Acta Geol Hun 28, 29–48.

Birkeland, P.W., 1984. In: Soils and Geomorphology. Oxford University Press. https://doi.org/10.1017/S0016756800031617.

Błażejowski, B., Pszczółkowski, A., Grabowski, J., Wierzbowski, H., Deconinck, J.F., Olempska, E., Teodorski, A., Nawrocki, J., 2023. Integrated stratigraphy and clay mineralogy of the Owadów-Brzezinki section (Lower–Upper Tithonian transition, central Poland): implications for correlations between the Boreal and the Tethyan domains and palaeoclimate. J. Geol. Soc. London 180 (2). https://doi.org/10.1144/jgs2022-073 jgs2022-073.

Borst, A.M., Smith, M.P., Finch, A.A., Estrade, G., Villanova-de-Benavent, C., Nason, P., Marquis, E., Horsburgh, N.J., Goodenough, K.M., Xu, C., Kynický, J., Geraki, K., 2020. Adsorption of rare earth elements in regolith-hosted clay deposits. Nat. Commun. 11, 1–15. https://doi.org/10.1038/s41467-020-17801-5.

Bowell, R.J., 1994. Sorption of arsenic by iron oxides and oxyhydroxides in soils. Appl. Geochem. 9, 279–286. https://doi.org/10.1016/0883-2927(94)90038-8.

Bower, W.R., Morris, K., Livens, F.R., Mosselmans, J.F.W., Fallon, C.M., Fuller, A.J., Natrajan, L., Boothman, C., Lloyd, J.R., Utsunomiya, S., Grolimund, D., Ferreira Sanchez, D., Jilbert, T., Parker, J., Neill, T.S., Law, G.T.W., 2019. Metaschoepite dissolution in sediment column systems – implications for uranium speciation and transport. Environ. Sci. Tech. 53, 9915–9925. https://doi.org/10.1021/acs.est.9b02292.

Braun, J.J., Viers, J., Dupré, B., Polve, M., Ndam, J., Muller, J.P., 1998. Solid/liquid REE fractionation in the lateritic system of Goyoum, East Cameroon: the implication for the present dynamics of the soil covers of the humid tropical regions. Geochim. Cosmochim. Acta 62, 273–299. https://doi.org/10.1016/S0016-7037(97)00344-X.

Brlek, M., Gaynor, S.P., Mongelli, G., Bauluz, B., Sinisi, R., Brčić, V., Peytcheva, I., Mišur, I., Tapster, S., Trinajstić, N., Laita, E., Yuste, A., Šuica, S., Grizelj, A., Kukoč, D., Schaltegger, U., 2021. Karst bauxite formation during Miocene Climatic

Optimum (central Dalmatia, Croatia): mineralogical, compositional and geochronological perspectives. Int. J. Earth Sci. 110, 2899–2922. https://doi.org/10.1007/s00531-021-02091-z.

Calagari, A.A., Abedini, A., 2007. Geochemical investigations on Permo-Triassic bauxite horizon at Kanisheeteh, east of Bukan, West-Azarbaidjan, Iran. J. Geochem. Explor. 94, 1–18. https://doi.org/10.1016/j.gexplo.2007.04.003.

Canfield, D.E., Raiswell, R., Westrich, J.T., Reaves, C.M., Berner, R.A., 1986. The use of chromium reduction in the analysis of reduced inorganic sulfur in sediments and shales. Chem. Geol. 54 (1–2), 149–155. https://doi.org/10.1016/0009-2541(86)90078-1.

Cao, X., Chen, Y., Wang, X., Deng, X., 2001. Effects of redox potential and pH value on the release of rare earth elements from soil. Chemosphere 44, 655–661. https://doi.org/10.1016/S0045-6535(00)00492-6.

Chanvry, E., Marchand, E., Lopez, M., Séranne, M., Le Saout, G., Vinches, M., 2020. Tectonic and climate control on allochthonous bauxite deposition. Example from the mid-Cretaceous Villeveyrac basin, southern France. Sed. Geol. 407, 105727. https://doi.org/10.1016/j.sedgeo.2020.105727.

Chen, J., Wang, Q., Zhang, Q., Carranza, E.J.M., Wang, J., 2018. Mineralogical and geochemical investigations on the iron-rich gibbsitic bauxite in Yongjiang basin, SW China. J. Geochem. Explor. 188. https://doi.org/10.1016/j.gexplo.2018.02.007.

Coelho, M.R., Vidal-Torrado, P., 2000. Cerium (Ce) in some nodular ferricretes developed in soils of the Adamantina Formation. Sci. Agric. 57, 329–336. https://doi.org/10.1590/S0103-90162000000200021.

Combes, P.-J., Bardossy, G., 1995. Geodynamics of bauxites in the Tethyan realm. In: Nairn, A.E.M., Ricou, L.E., Vrielynck, B., Dercourt, J. (Eds.), The Tethys Ocean. Springer, Boston, MA. https://doi.org/10.1007/978-1-4899-1558-0_11.

Coppin, F., Berger, G., Bauer, A., Castet, S., Loubet, M., 2002. Sorption of lanthanides on smectite and kaolinite. Chem. Geol. 182, 57–68. https://doi.org/10.1016/S0009-2541(01)00283-2.

D'Argenio, B., Mindszenty, A., 1992. Tectonic and climatic control on paleokarst and bauxites. Giorn. Geol. 54, 207–218.

D'Argenio, B., Mindszenty, A., 1995. Bauxites and related paleokarst: tectonic and climatic event markers at regional unconformities. Eclogae Geol. Helv. 88, 453–499.

De Campos, D.S., Monteiro, H.S., Vasconcelos, P.M., Farley, K.A., Silva, A.C., Vidal-Torrado, P., 2023. A new model of bauxitization in quartzitic landscapes: a case study from the Southern Espinhaço Range (Brazil). Earth Surf. Proc. Land. 48, 2788–2807. https://doi.org/10.1002/esp.5660.

Dia, A., Gruau, G., Olivié-Lauquet, G., Riou, C., Molénat, J., Curmi, P., 2000. The distribution of rare earth elements in groundwaters: assessing the role of source-rock composition, redox changes and colloidal particles. Geochim. Cosmochim. Acta 64, 4131–4151. https://doi.org/10.1016/S0016-7037(00)00494-4.

Doebelin, N., Kleeberg, R., 2015. Profex: A graphical user interface for the Rietveld refinement program BGMN. J. Appl. Cryst. 48, 1573–1580. https://doi.org/10.1107/S1600576715014685.

Dozet, S., Mišić, M., Žuža, T., 1993. New data on the stratigraphic position, mineralogy and chemistry of Nanos bauxite deposits and adjacent carbonate rocks, Slovenia. Geol. Croat. 46, 233–241.

Duncan, T., Shaw, T.J., 2003. The mobility of Rare Earth Elements and Redox Sensitive Elements in the groundwater/seawater mixing zone of a shallow coastal aquifer. Aquat. Geochem. 9, 233–255. https://doi.org/10.1023/B:AQUA.0000022956.20338.26.

Durn, G., Ottner, F., Slovenec, D., 1999. Mineralogical and geochemical indicators of the polygenetic nature of terra rossa in Istria, Croatia. Geoderma 91, 125–150. https://doi.org/10.1016/S0016-7061(98)00130-X.

Durn, G., Ottner, F., Tišljar, J., Mindszenty, A., Barudžija, U., 2003. Regional subaerial unconformities in shallow-marine carbonate sequences of istria: sedimentology, mineralogy, geochemistry and micromorphology of associated bauxites, palaeosols and pedo-sedimentary complexes. In: Vlahović, I., Tišljar, J. (Eds.), Field Trip Guidebook: Evolution of Depositional Environments from the Palaeozoic to the Quaternary in the Karst Dinarides and the Pannonian Basin. 22nd IAS Meeting of Sedimentology. Institute of Geology Zagreb, Zagreb, pp. 209–255.

Durn, G., Mindszenty, A., Tišljar, J., Mileusnić, M., 2006. Clay mineralogy of bauxites and palaeosols in Istria formed during regional subaerial exposures of the Adriatic Carbonate Platform. In: Vlahović, I., Tibljaš, D., Durn, G. (Eds.), 3rd Mid-European Clay Conference: Field Trip Guidebook. University of Zagreb, Faculty of Science and Faculty of Mining, Geology and Petroleum Engineering, Zagreb, Croatia, pp. 3–30.

Durn, G., Perković, I., Mileusnić, M., Vlahović, I., Ružičić, S., Matešić, D., Cvetko Tešović, B., Martinuš, M., Rubinić, V., Razum, I., Šegvić, B., Mihovilović, M., Zvocak, S., 2023. Field trip A2 – Red Istria : Western Istrian Anticline as an ideal natural laboratory for the study of the regional unconformities in carbonate rocks. In: Fio Firi, K., Čobić, A. (Eds.), Excursion Guide-Book / 7th Croatian Geological Congress with International Participation. Hrvatski geološki institut, Zagreb, pp. 33–58.

Economou-Eliopoulos, M., Kontou, M., Megremi, I., 2022. Biogeochemical redox processes controlling the element cycling: insights from karst-type bauxite, Greece. Minerals 12, 446. https://doi.org/10.3390/min12040446.

Elders, W.A., Hoagland, J.R., McDowell, S.D., Cobo, J.M., 1979. Hydrothermal mineral zones in the geothermal reservoir of Cerro Prieto. Geothermics. https://doi.org/10.1016/0375-6505(79)90042-7.

Ellahi, S.S., Taghipour, B., Zarasvandi, A., Bird, M.I., Somarin, A.K., 2015. Mineralogy, geochemistry and stable isotope studies of the Dopolan bauxite deposit, Zagros mountain, Iran. Minerals 6. https://doi.org/10.3390/min6010011.

Ellahi, S.S., Taghipour, B., Nejadhadad, M., 2017. The role of organic matter in the formation of high-grade Al deposits of the Dopolan karst type bauxite, Iran: mineralogy, geochemistry, and sulfur isotope data. Minerals 7. https://doi.org/10.3390/min7060097.

Flügel, E., 2004. In: Microfacies of Carbonate Rocks. Springer, Berlin. https://doi.org/10.1007/978-3-662-08726-8.

Frakes, L.A., Francis, J.E., Syktus, J.I., 1992. Climate modes of the Phanerozoic. Cambridge University Press, Cambridge, UK. https://doi.org/10.1016/0037-0738(94)90045-0.

Fuller, A.J., Leary, P., Gray, N.D., Davies, H.S., Mosselmans, J.F.W., Cox, F., Robinson, C.H., Pittman, J.K., McCann, C.M., Muir, M., Graham, M.C., Utsunomiya, S., Bower, W.R., Morris, K., Shaw, S., Bots, P., Livens, F.R., Law, G.T.W., 2020. Organic complexation of U(VI) in reducing soils at a natural analogue site: implications for uranium transport. Chemosphere 254, 126859. https://doi.org/10.1016/j.chemosphere.2020.126859.

Gamaletsos, P.N., Godelitsas, A., Kasama, T., Church, N.S., Douvalis, A.P., Göttlicher, J., Steininger, R., Boubnov, A., Pontikes, Y., Tzamos, E., Bakas, T., Filippidis, A., 2017. Nano-mineralogy and geochemistry of high-grade diasporic karst-type bauxite from Parnassos–Ghiona mines, Greece. Ore Geol. Rev. 84, 228–244. https://doi.org/10.1016/j.oregeorev.2016.11.009.

Gardner, L.R., 1970. A Chemical model for the origin of gibbsite from kaolinite. Am Min 55, 1380–1389.

Georgiadis, A., Dietel, J., Dohrmann, R., Rennert, T., 2020. What are the nature and formation conditions of hydroxy-interlayered minerals (HIMs) in soil? J. Plant. Nut. Soil Sci. 83 (1), 12–26. https://doi.org/10.1002/jpln.201900283.

Gil-Delgado, A., Cruset, D., Oms, O., Botero, E., Ibáñez-Insa, J., Delclòs, X., Sellés, A., Galobart, À., Mercedes-Martín, R., 2023. Geochemical approach for decoding the paleoenvironmental and depositional evolution of a coastal lacustrine Konservat-Lagerstätte (Early Cretaceous, south-Central Pyrenees). Sed. Geol. 453, 106440. https://doi.org/10.1016/j.sedgeo.2023.106440.

Giresse, P., Wiewióra, A., 2001. Stratigraphic condensed deposition and diagenetic evolution of green clay minerals in deep water sediments on the Ivory Coast–Ghana Ridge. Mar. Geol. 179, 51–70. https://doi.org/10.1016/S0025-3227(01)00193-1.

Goldberg, S., Forster, H.S., Godfrey, C.L., 1996. Molybdenum adsorption on oxides, clay minerals, and soils. Soil Sci. Soc. Am. J. 60, 425–432. https://doi.org/10.2136/sssaj1996.03615995006000020013x.

Graulis, S., Chateigner, D., Downs, R.T., Yokochi, A.F.T., Quirós, M., Lutterotti, L., Manakova, E., Butkus, J., Moeck, P., Le Bail, A., 2009. Crystallography Open Database – an open-access collection of crystal structures. J. Appl. Cryst. 42, 726–729. https://doi.org/10.1107/S0021889809016690.

Hao, W., Flynn, S.L., Kashiwabara, T., Alam, M.S., Bandara, S., Swaren, L., Robbins, L.J., Alessi, D.S., Konhauser, K.O., 2019. The impact of ionic strength on the proton reactivity of clay minerals. Chem. Geol. 529, 119294. https://doi.org/10.1016/j.chemgeo.2019.119294.

Haq, B.U., 2018. Jurassic sea-level variations: a reappraisal. GSA Today 28, 4–10. https://doi.org/10.1130/GSATG359A.1.

Haq, B.U., Al-Qahtani, A.M., 2005. Phanerozoic cycles of sea-level change on the Arabian platform. GeoArabia 10, 127–160. https://doi.org/10.2113/geoarabia1002127.

Hesselbo, S.P., Deconick, J.-F., Huggett, J.M., Morgans-Bell, H.S., 2009. Late Jurassic palaeoclimatic change from clay mineralogy and gamma-ray spectrometry of the Kimmeridge Clay, Dorset, UK. J. Geol. Soc. London 166, 1123–1133. https://doi.org/10.1144/0016-76492009-070.

Hu, W., Ran, J., Dong, L., Du, Q., Ji, M., Yao, S., Sun, Y., Gong, C., Hou, Q., Gong, H., Chen, R., Lu, J., Xie, S., Wang, Z., Huang, H., Li, X., Xiong, J., Xia, R., Wei, M., Zhao, D., Zhang, Y., Li, J., Yang, H., Wang, X., Deng, Y., Sun, Y., Li, H., Zhang, L., Chu, Q., Li, X., Aqeel, M., Manan, A., Akram, M.A., Liu, X., Li, R., Li, F., Hou, C., Liu, J., He, J.S., An, L., Bardgett, R.D., Schmid, B., Deng, J., 2021. Aridity-driven shift in biodiversity–soil multifunctionality relationships. Nat. Commun. 12, 5350. https://doi.org/10.1038/s41467-021-25641-0.

Jackson, M.L., 1979. Soil Chemical Analysis – Advanced Course. Soil Science Department. University of Wisconsin, Madison.

Kalaitzidis, S., Siavalas, G., Skarpelis, N., Araujo, C.V., Christanis, K., 2010. Late Cretaceous coal overlying karstic bauxite deposits in the Parnassos–Ghiona Unit, Central Greece: coal characteristics and depositional environment. Int. J. Coal Geol. 81, 211–226. https://doi.org/10.1016/j.coal.2009.06.005.

Kalatha, S., Perraki, M., Economou-Eliopoulos, M., Mitsis, I., 2017. On the origin of bastnaesite-(La, Nd, Y) in the Nissi (Patitira) bauxite laterite deposit, Lokris, Greece. Minerals 7. https://doi.org/10.3390/min7030045.

Kawabe, I., Ohta, A., Ishii, S., Tokumura, M., Miyauchi, K., 1999. REE partitioning between Fe-Mn oxyhydroxide precipitates and weakly acid NaCl solutions: convex tetrad effect and fractionation of Y and Sc from heavy lanthanides. Geochem. J. 33, 167–179. https://doi.org/10.2343/geochemj.33.167.

Kelemen, P., Dunkl, I., Csillag, G., Mindszenty, A., von Eynatten, H., Józsa, S., 2017. Tracing multiple resedimentation on an isolated karstified plateau: the bauxite-bearing Miocene red clay of the Southern Bakony Mountains, Hungary. Sed. Geol. 358, 84–96. https://doi.org/10.1016/j.sedgeo.2017.07.005.

Kelemen, P., Dunkl, I., Csillag, G., Mindszenty, A., Józsa, S., Fodor, L., von Eynatten, H., 2023. Origin, timing and paleogeographic implications of Paleogene karst bauxites in the northern Transdanubian range, Hungary. Int. J. Earth Sci. 112, 243–264. https://doi.org/10.1007/s00531-022-02249-3.

Khosravi, M., Vérard, C., Abedini, A., 2021. Palaeogeographic and geodynamic control on the Iranian karst-type bauxite deposits. Ore Geol. Rev. 139, 104589. https://doi.org/10.1016/j.oregeorev.2021.104589.

Kiss, A.B., Keresztury, G., Farkas, L., 1980. Raman and i.r. spectra and structure of boehmite (γ-AlOOH). Evidence for the recently discarded $D^{17}2h$ space group. Spectrochim. Acta A 36, 653–658. https://doi.org/10.1016/0584-8539(80)80024-9.

Koppi, A.J., Edis, R., Field, D.J., Geering, H.R., Klessa, D.A., Cockayne, D.J.H., 1996. Rare earth element trends and cerium–uranium–manganese associations in weathered rock from Koongarra, Northern Territory, Australia. Geochim. Cosmochim. Acta 60, 1695–1707. https://doi.org/10.1016/0016-7037(96)00047-6.

Kovács, J., Raucsik, B., Varga, A., Újvári, G., Varga, G., Ottner, F., 2013. Clay mineralogy of red clay deposits from the central Carpathian Basin (Hungary): implications for Plio-Pleistocene chemical weathering and palaeoclimate. Turk. J. Earth Sci. 22, 414–426. https://doi.org/10.3906/yer-1201-4.

Laskou, M., Economou-Eliopoulos, M., 2007. The role of microorganisms on the mineralogical and geochemical characteristics of the Parnassos–Ghiona bauxite deposits, Greece. J. Geochem. Explor. 93, 67–77. https://doi.org/10.1016/j.gexplo.2006.08.014.

Laskou, M., Economou-Eliopoulos, M., 2013. Bio-mineralization and potential biogeochemical processes in bauxite deposits: genetic and ore quality significance. Mineral. Petrol. 107, 471–486. https://doi.org/10.1007/s00710-012-0257-z.

Laveuf, C., Cornu, S., Juillot, F., 2008. Rare earth elements as tracers of pedogenetic processes. Comptes Rendus – Geosci. 340, 523–532. https://doi.org/10.1016/j.crte.2008.07.001.

Laveuf, C., Cornu, S., Guilherme, L.R.G., Guerin, A., Juillot, F., 2012. The impact of redox conditions on the rare earth element signature of redoximorphic features in a soil sequence developed from limestone. Geoderma 170, 25–38. https://doi.org/10.1016/j.geoderma.2011.10.014.

Liankai, Z., Hongbing, J., Shijie, W., Gang, L., Xiuming, L., Xiao, W., QuocDinh, N., DaiTrung, N., 2020. Geochemical implications of rare earth elements in terra rossa in tropical karst area: a case study in northern Vietnam. Appl. Sci. (Switzerland) 10, 858. https://doi.org/10.3390/app10030858.

Lin, R., Bank, T., Roth, E., Granite, E., Soong, Y., 2017. Organic and inorganic association of rare earth elements in coal. In: 34th Annual International Pittsburgh Coal Conference: Coal – Energy Environment and Sustainable Development, PCC 2017, pp. 1–20.

Lucas, Y., 2001. The role of plants in controlling rates and products of weathering: Importance of biological pumping. Annu. Rev. Earth Planet. Sci. 29, 135–163. https://doi.org/10.1146/annurev.earth.29.1.135.

Madejová, J., Komadel, P., 2001. Baseline studies of the Clay Minerals Society source clays: infrared methods. Clays Clay Min. 49 (5), 410–432.

Majidzadeh, H., Uzun, H., Ruecker, A., Miller, D., Vernon, J., Zhang, H., Bao, S., Tsui, M. T.K., Karanfil, T., Chow, A.T., 2017. Extreme flooding mobilized dissolved organic matter from coastal forested wetlands. Biogeochemistry 136, 293–309. https://doi.org/10.1007/s10533-017-0394-x.

Maksimović, Z., Pantó, G., 1991. Contribution to the geochemistry of the rare earth elements in the karst-bauxite deposits of Yugoslavia and Greece. Geoderma 51. https://doi.org/10.1016/0016-7061(91)90067-4.

Maksimović, Z., Mindszenty, A., Panto, G., 1991. Contribution to the geochemistry of Hungarian karst bauxites and the allochthony/autochthony problem. Acta Geol. Hun. 34, 317–334.

Mameli, P., Mongelli, G., Oggiano, G., Dinelli, E., 2007. Geological, geochemical and mineralogical features of some bauxite deposits from Nurra (Western Sardinia, Italy): insights on conditions of formation and parental affinity. Int. J. Earth Sci. 96, 887–902. https://doi.org/10.1007/s00531-006-0142-2.

Mehra, O.P., Jackson, M.L., 1960. Iron oxide removal from soils and clays by a dithionite-citrate system buffered with sodium bicarbonate. Clays Clay Min. 7, 317–327.

Meunier, A., El Albani, A., 2007. The glauconite-Fe-illite-Fe-smectite problem: a critical review. Terra Nova 19 (2), 95–104. https://doi.org/10.1111/j.1365-3121.2006.00719.x.

Mindszenty, A., 2016. Bauxites: feedbacks of system Earth at greenhouse times. Geol. Croat 69, 79–87. https://doi.org/10.4154/gc.2016.07.

Mindszenty, A., D'Argenio, B., Aiello, G., 1995. Lithospheric bulges recorded by regional unconformities. The Case of Mesozoic–Tertiary Apulia. Tectonophysics 252, 137–161. https://doi.org/10.1016/0040-1951(95)00091-7.

Molina, J.M., Ruiz-Ortiz, P.A., Vera, J.A., 1991. Jurassic karst bauxites in the Subbetic, Betic Cordillera, southern Spain. Acta Geol. Hung. 34, 163–178.

Mongelli, G., 1997. Ce-anomalies in the textural components of Upper Cretaceous karst bauxites from the Apulian Carbonate Platform (southern Italy). Chem. Geol. 140, 69–79. https://doi.org/10.1016/S0009-2541(97)00042-9.

Mongelli, G., Boni, M., Buccione, R., Sinisi, R., 2014. Geochemistry of the Apulian karst bauxites (southern Italy): chemical fractionation and parental affinities. Ore Geol. Rev. 63, 9–21. https://doi.org/10.1016/j.oregeorev.2014.04.012.

Mongelli, G., Buccione, R., Sinisi, R., 2015. Genesis of autochthonous and allochthonous Apulian karst bauxites (Southern Italy): climate constraints. Sed. Geol. 325, 168–176. https://doi.org/10.1016/j.sedgeo.2015.06.005.

Mongelli, G., Boni, M., Oggiano, G., Mameli, P., Sinisi, R., Buccione, R., Mondillo, N., 2017. Critical metals distribution in Tethyan karst bauxite: the Cretaceous Italian ores. Ore Geol. Rev. 86, 526–536. https://doi.org/10.1016/j.oregeorev.2017.03.017.

Mongelli, G., Mameli, P., Sinisi, R., Buccione, R., Oggiano, G., 2021. REE and other critical raw materials in Cretaceous Mediterranean-type bauxite: the case of the Sardinian ore (Italy). Ore Geol. Rev. 139, 104559. https://doi.org/10.1016/j.oregeorev.2021.104559.

Moore, D.M., Reynolds, R.C. jr, 1997. X-Ray Diffraction and the Identification and Analysis of Clay Minerals, second ed., Oxford University Press.

Neaman, A., Mouélé, F., Trolard, F., Bourrié, G., 2004. Improved methods for selective dissolution of Mn oxides: applications for studying trace element associations. Appl. Geochem. 19, 973–979. https://doi.org/10.1016/j.apgeochem.2003.12.002.

Newsome, L., Morris, K., Shaw, S., Trivedi, D., Lloyd, J.R., 2015. The stability of microbially reduced U(IV); impact of residual electron donor and sediment ageing. Chem. Geol. 409, 125–135. https://doi.org/10.1016/j.chemgeo.2015.05.016.

Ni, Y., Hughes, J.M., Mariano, A.N., 1993. The atomic arrangement of bastnasite-(Ce), Ce $(CO_3)F$, and structural elements of synchysite-(Ce), rontgenite-(Ce), and parisite-(Ce). Am. Min. 78, 415–418.

Ni, Y., Post, J.E., Hughes, J.M., 2000. The crystal structure of parisite-(Ce), $Ce_2CaF_2(CO_3)_3$. Am Min 85, 251–258. https://doi.org/10.2138/am-2000-0126.

Odin, G.S., Matter, A., 1981. De glauconiarum origine. Sedimentology 28, 121–151. https://doi.org/10.1111/j.1365-3091.1981.tb01925.x.

Ohta, A., Kawabe, I., 2001. REE(III) adsorption onto Mn dioxide (δ-MnO_2) and Fe oxyhydroxide: Ce(III) oxidation by δ-MnO_2. Geochim. Cosmochim. Acta 65, 695–703. https://doi.org/10.1016/S0016-7037(00)00578-0.

Parfitt, R.L., Smart, R.st.C., 1978. The mechanism of sulfate adsorption on iron oxides. Soil Sci. Soc. Am. J. 42, 48–50. https://doi.org/10.2136/sssaj1978.03615995004200010011x.

Pellenard, P., Nomade, S., Martire, L., De Oliveira Ramalho, F., Monna, F., Guillou, H., 2013. The first ^{40}Ar–^{39}Ar date from Oxfordian ammonite-calibrated volcanic layers (bentonites) as a tie-point for the Late Jurassic. Geol. Mag. 150, 1136–1142. https://doi.org/10.1017/S0016756813000605.

Perković, I., Cvetko Tešović, B., Martinuš, M., Škapin, S.D., Vlahović, I., Matešić, D., Durn, G., 2024. Glauconitisation of an Upper Jurassic palaeosol: case study of the Zlatni Rt, Istria. Croatia. Catena 238, 107841. https://doi.org/10.1016/j.catena.2024.107841.

Picotti, V., Cobianchi, M., 2017. Jurassic stratigraphy of the Belluno Basin and Friuli Platform: a perspective on far-field compression in the Adria passive margin. Swiss J. Geosci. 110, 833–850. https://doi.org/10.1007/s00015-017-0280-5.

Poulton, S.W., 2021. In: The Iron Speciation Paleoredox Proxy. Cambridge University Press. https://doi.org/10.1017/9781108847148.

Poulton, S.W., Canfield, D.E., 2005. Development of a sequential extraction procedure foriron: Implications for iron partitioning in continentally derived particulates. Chem. Geol. 214 (3–4), 209–221. https://doi.org/10.1016/j.chemgeo.2004.09.003.

Poulton, S.W., Canfield, D.E., 2011. Ferruginous conditions: a dominant feature of the ocean through Earth's history. Elements 7, 107–112. https://doi.org/10.2113/gselements.7.2.107.

Quinn, K.A., Byrne, R.H., Schijf, J., 2006. Sorption of yttrium and rare earth elements by amorphous ferric hydroxide: influence of pH and ionic strength. Marine Chem 99, 128–150. https://doi.org/10.1016/j.marchem.2005.05.011.

Radusinović, S., Papadopoulos, A., 2021. The potential for REE and associated critical metals in karstic bauxites and bauxite residue of Montenegro. Minerals 11. https://doi.org/10.3390/min11090975.

Radusinović, S., Jelenković, R., Pačevski, A., Simić, V., Božović, D., Holclajtner-Antunović, I., Životić, D., 2017. Content and mode of occurrences of rare earth elements in the Zagrad karstic bauxite deposit (Nikšić area, Montenegro). Ore Geol. Rev. 80, 406–428. https://doi.org/10.1016/j.oregeorev.2016.05.026.

Rankin, P.C., Childs, C.W., 1976. Rare-earth elements in iron-manganese concretions from some New Zealand soils. Chem. Geol. 18, 55–64. https://doi.org/10.1016/0009-2541(76)90061-9.

Rasmussen, K., Neumann, A.C.N., 1988. Holocene overprint of Pleistocene paleokarst: bight of Abaco, Bahamas. In: James, N.P., Choquette, P.W. (Eds.), Paleokarst. Springer-Verlag, pp. 132–148.

Reinhardt, N., Proenza, J.A., Villanova-De-Benavent, C., Aiglsperger, T., Bover-Arnal, T., Torró, L., Salas, R., Dziggel, A., 2018. Geochemistry and mineralogy of rare earth elements (REE) in bauxitic ores of the Catalan coastal range, NE Spain. Minerals 8. https://doi.org/10.3390/min8120562.

Ruffell, A., McKinley, J.M., Worden, R.H., 2002. Comparison of clay mineral stratigraphy to other proxy palaeoclimate indicators in the Mesozoic of NW Europe. Philos. Trans. R. Soc. London, Ser. A 360 (1793), 675–693. https://doi.org/10.1098/rsta.2001.0961.

Russell, J.D., Fraser, A.R., 1994. Infrared methods. In: Clay Mineralogy: Spectroscopic and Chemical Determinative Methods. Springer Netherlands, Dordrecht. pp. 11–67. https://doi.org/10.1007/978-94-011-0727-3_2.

Sahrawat, K.L., 2003. Organic matter accumulation in submerged soils. Adv. Agron. 81, 169–201. https://doi.org/10.1016/S0065-2113(03)81004-0.

Šćavničar, B., Nikler, L., 1976. Vitric tuff in Upper Jurassic Lemeš-deposits of Mt. Velika Kapela (Croatia). Geol Vjes 29, 269–275.

Schmid, S.M., Bernoulli, D., Fügenschuh, B., Matenco, L., Schefer, S., Schuster, R., Tischler, M., Ustaszewski, K., 2008. The Alpine–Carpathian–Dinaridic orogenic system: correlation and evolution of tectonic units. Swiss J. Geosci. 101, 139–183. https://doi.org/10.1007/s00015-008-1247-3.

Schmid, S.M., Fügenschuh, B., Kounov, A., Maţenco, L., Nievergelt, P., Oberhänsli, R., Pleuger, J., Schefer, S., Schuster, R., Tomljenović, B., Ustaszewski, K., van Hinsbergen, D.J.J., 2020. Tectonic units of the alpine collision zone between Eastern Alps and Western Turkey. Gondw. Res. 78, 308–374. https://doi.org/10.1016/j.gr.2019.07.005.

Scott, C., Slack, J.F., Kelley, K.D., 2017. The hyper-enrichment of V and Zn in black shales of the Late Devonian–Early Mississippian Bakken Formation (USA). Chem. Geol. 452, 24–33. https://doi.org/10.1016/j.chemgeo.2017.01.026.

Shaheen, S.M., Rinklebe, J., Frohne, T., White, J.R., DeLaune, R.D., 2016. Redox effects on release kinetics of arsenic, cadmium, cobalt, and vanadium in Wax Lake Deltaic freshwater marsh soils. Chemosphere 150, 740–748. https://doi.org/10.1016/j.chemosphere.2015.12.043.

Shen, Q., Demisie, W., Zhang, S., Zhang, M., 2020. The association of heavy metals with iron oxides in the aggregates of naturally enriched soil. Bull. Environ. Contam. Toxicol. 104, 144–148. https://doi.org/10.1007/s00128-019-02739-2.

Šinkovec, B., 1974. Jurski Boksiti Zapadne Istre. Geol. Vjes 27, 217–226.

Šinkovec, B., Sakač, K., Durn, G., 1994. Pyritized bauxites from Minjera, Istria, Croatia. Nat. Croat. 3, 41–65.

Slonimskaya, M.V., Besson, G., Dainyak, L.G., Tchoubar, C., Drits, V.A., 1986. Interpretation of the IR spectra of celadonites and glauconites in the region of OH-stretching frequencies. Clay Miner. 21, 377–388.

Steiner, T.M.C., Gawlick, H.J., Melcher, F., Schlagintweit, F., 2021. Ophiolite derived material as parent rocks for Late Jurassic bauxite: evidence for Tithonian unroofing in the Northern Calcareous Alps (Eastern Alps, Austria). Int. J. Earth. Sci. 110, 1847–1862. https://doi.org/10.1007/s00531-021-02044-6.

Środoń, J., 1980. Precise identification of illite/smectite interstratifications by X-ray powder diffraction. Clays Clay Miner. 28, 401–411.

Środoń, J., 1981. X-ray identification of randomly interstratified illite–smectite in mixtures with discrete illite. Clay Miner. 16, 297–304.

Środoń, J., 2006. Identification and Quantitative Analysis of Clay Minerals. In: Bergaya, F, Gerhard, L. (Eds.), Handbook of clay science. Elsevier, pp. 25–49. https://doi.org/10.1016/S1572-4352(05)01028-7.

Stoops, G., 2021. Guidelines for Analysis and Description of Soil and Regolith Thin Sections. John Wiley and Sons.

Taylor, S.R., McLennan, S.M., 1985. The Continental Crust: Its Composition and Evolution. Blackwell, Oxford.

Tišljar, J., 1986. Postanak crnih oblutaka i ulomaka (“black pebbles”) u periplimskimvapnencima titona zapadne Istre i barema otoka Mljeta. Geol. Vj. 39, 75–94.

Tomašić, N., Čobić, A., Bedeković, M., Miko, S., Ilijanić, N., Gizdavec, N., Matošević, M., 2021. Rare earth elements enrichment in the upper Eocene Tošići-Dujići bauxite deposit, Croatia, and relation to ree mineralogy, parent material and weathering pattern. Minerals 11. https://doi.org/10.3390/min11111260.

Trabelsi, K., Sames, B., Wagreich, M., Kázmér, M., Mindszenty, A., Martín-Closas, C., 2021. A new diverse charophyte flora and biozonation of the Eocene bauxite cover-sequence at Gánt (Vértes Hills, Hungary). J. Syst. Palaeontol. 19, 541–563. https://doi.org/10.1080/14772019.2021.1938264.

Trojanović, D., 1973. Jurski boksiti zapadne Istre. In: II. Jugoslavenski simpozij o istraživanju i eksploataciji boksita. Tuzla. pp. 53–66.

van Hinsbergen, D.J.J., Torsvik, T.H., Schmid, S.M., Maţenco, L.C., Maffione, M., Vissers, R.L.M., Gürer, D., Spakman, W., 2020. Orogenic architecture of the Mediterranean region and kinematic reconstruction of its tectonic evolution since the Triassic. Gondw. Res. 81, 79–229. https://doi.org/10.1016/j.gr.2019.07.009.

Velić, I., Tišljar, J., 1988. Litostratigrafske jedinice u dogeru i malmu zapadne Istre (zapadna Hrvatska, Jugoslavija). Geol Vjes 41, 25–49.

Velić, I., Vlahović, I., Tišljar, J., 1994. Late Jurassic lateral and vertical facies distribution : from peritidal and inner carbonate ramps to perireefal and peritidal deposits in SE Gorski Kotar (Croatia). Géol. Médit. 21, 177–180. https://doi.org/10.3406/geolm.1994.1558.

Velić, I., Matičec, D., Tišljar, J., Vlahović, I., 1995. Opći prikaz geološke građe Istre (A review of the geology of Istria). In: 1st Croatian Geological Congress, Excursion Guidebook. pp. 5–30.

Velić, I., Tišljar, J., Vlahović, I., Velić, J., Koch, G., Matičec, D., 2002. Palaeogeographic variability and depositional environments of the Upper Jurassic carbonate rocks of velika Kapela Mt. (Gorski Kotar area, Adriatic Carbonate Platform, Croatia). Geol. Croat 55, 121–138.

Villanova-de-Benavent, C., Proenza, J.A., Torró, L., Aiglsperger, T., Domènech, C., Domínguez-Carretero, D., Llovet, X., Suñer, P., Ramírez, A., Rodríguez, J., 2023. REE ultra-rich karst bauxite deposits in the Pedernales Peninsula, Dominican Republic: mineralogy of REE phosphates and carbonates. Ore Geol. Rev. 157, 105422. https://doi.org/10.1016/j.oregeorev.2023.105422.

Vind, J., Malfliet, A., Blanpain, B., Tsakiridis, P.E., Tkaczyk, A.H., Vassiliadou, V., Panias, D., 2018. Rare earth element phases in bauxite residue. Minerals 8. https://doi.org/10.3390/min8020077.

Vitzthum, M.A.J., Gawlick, H.J., Sachsenhofer, R.F., Neumeister, S., 2022. Changing depositional environments in the semi-restricted Late Jurassic Lemeš Basin (Outer Dinarides; Croatia). Facies 68, 2. https://doi.org/10.1007/s10347-021-00640-1.

Vlahović, I., Velić, I., Tišljar, J., Matičec, D., 2001. Malmian palaeogeography of the Adriatic Carbonate Platform as a consequence of the synsedimentary tectonics. In: Velić, I., Dragičević, I. (Eds.), The First Scientific Meeting, Carbonate Platform or Carbonate Platforms of Dinarides, Abstract Book, pp. 51–54.

Vlahović, I., Tišljar, J., Velić, I., Matičec, D., Skelton, P., Korbar, T., Fuček, L., 2003. Main events recorded in the sedimentary succession of the Adriatic Carbonate Platform from Oxfordian to the upper Santonian in Istria (Croatia). In: Field Trip Guidebook : Evolution of Depositional Environments from the Palaeozoic to the Quaternary in the Karst Dinarides and the Pannonian Basin / 22nd IAS Meeting of Sedimentology. Institute of Geology, Zagreb, Croatia, pp. 19–58.

Vlahović, I., Tišljar, J., Velić, I., Matičec, D., 2005. Evolution of the Adriatic Carbonate Platform: palaeogeography, main events and depositional dynamics. Palaeogeogr. Palaeoclimatol. Palaeoecol. 220, 333–360. https://doi.org/10.1016/j.palaeo.2005.01.011.

Vlahović, I., Velić, I., Matičec, D., 2023. A brief introduction to the geology of Istria. In: FioFiri, K., Čobić, A. (Eds.), Excursion Guide-book, 7th Croatian Geological Congress, 1–13. Hrvatski geološki institut.

Wang, X., Jiao, Y., Du, Y., Ling, W., Wu, L., Cui, T., Zhou, Q., Jin, Z., Lei, Z., Weng, S., 2013. REE mobility and Ce anomaly in bauxite deposit of WZD area, Northern Guizhou, China. J. Geochem. Explor. 133, 103–117. https://doi.org/10.1016/j.gexplo.2013.08.009.

Wanty, R.B., Goldhaber, M.B., 1992. Thermodynamics and kinetics of reactions involving vanadium in natural systems: accumulation of vanadium in sedimentary rocks. Geochim. Cosmochim. Acta 56, 1471–1483. https://doi.org/10.1016/0016-7037(92)90217-7.

Warr, L.N., 2021. IMA–CNMNC approved mineral symbols. Min. Mag. 85 (3), 291–320.

Wei, T., Simko, V., 2017. R package “corrplot”: Visualization of a Correlation Matrix.

Weng, L., Van Riemsdijk, W.H., Hiemstra, T., 2012. Factors controlling phosphate interaction with iron oxides. J. Environ. Qual. 41, 628–635. https://doi.org/10.2134/jeq2011.0250.

Wignall, P.B., Ruffell, A.H., 1990. The influence of a sudden climatic change on marine deposition in the Kimmeridgian of northwest Europe. J. Geol. Soc. London 147, 365–371. https://doi.org/10.1144/gsjgs.147.2.0365.

Xiao, J., Li, Y., Yang, H., Xu, J., Huang, M., 2021. Geochemistry of the Yudong bauxite deposit, south-eastern Guizhou, China: implications for conditions of formation and parental affinity. J. Geochem. Explor. 220, 106676. https://doi.org/10.1016/j.gexplo.2020.106676.

Xu, C., Kynický, J., Smith, M.P., Kopriva, A., Brtnický, M., Urubek, T., Yang, Y., Zhao, Z., He, C., Song, W., 2017. Origin of heavy rare earth mineralization in South China. Nat. Commun. 8, 14598. https://doi.org/10.1038/ncomms14598.

Yang, S., Wang, Q., Deng, J., Wang, Y., Kang, W., Liu, X., Li, Z., 2019. Genesis of karst bauxite-bearing sequences in Baofeng, Henan (China), and the distribution of critical metals. Ore Geol. Rev. 115, 103161. https://doi.org/10.1016/j.oregeorev.2019.103161.

Yang, S., Wang, Q., Liu, X., Kan, Z., Santosh, M., Deng, J., 2022. Global spatio-temporal variations and metallogenic diversity of karst bauxites and their tectonic, paleogeographic and paleoclimatic relationship with the Tethyan realm evolution. Earth Sci. Rev., 104184 https://doi.org/10.1016/j.earscirev.2022.104184.

Yuste, A., Bauluz, B., Mayayo, M.J., 2017. Origin and geochemical evolution from ferrallitized clays to karst bauxite: an example from the Lower Cretaceous of NE Spain. Ore Geol. Rev. 84, 67–79. https://doi.org/10.1016/j.oregeorev.2016.12.025.

Zarasvandi, A., Carranza, E.J.M., Ellahi, S.S., 2012. Geological, geochemical, and mineralogical characteristics of the Mandan and Deh-now bauxite deposits, Zagros Fold Belt, Iran. Ore Geol. Rev. 48, 125–138. https://doi.org/10.1016/j.oregeorev.2012.02.010.

Zhou, J., Yu, W., Wei, W., Yang, M., Du, Y., 2023. Provenance and tectonic evolution of bauxite deposits in the Tethys: perspective from random forest and logistic regression analyses. Geochem. Geophys. Geosyst. 24. https://doi.org/10.1029/2022GC010745.

Zviagina, B.B., Drits, V.A., Dorzhieva, O.V., 2020. Distinguishing features and identification criteria for K-dioctahedral 1M micas (Illite-aluminoceladonite and illite-glauconite-celadonite series) from middle-infrared spectroscopy data. Minerals 10. https://doi.org/10.3390/min10020153.